Planetary and Space Science 112 (2015) 98–114

Contents lists available at ScienceDirect

Planetary and Space Science

journal homepage: www.elsevier.com/locate/pss

Mars Advanced Radar for Subsurface and Ionospheric Sounding (MARSIS) after nine years of operation: A summary

R. Orosei [a,*], R.L. Jordan [b], D.D. Morgan [c], M. Cartacci [d], A. Cicchetti [d], F. Duru [c], D.A. Gurnett [c], E. Heggy [b], D.L. Kirchner [c], R. Noschese [d], W. Kofman [e,f], A. Masdea [g], J.J. Plaut [b], R. Seu [g], T.R. Watters [h], G. Picardi [g]

[a] Istituto di Radioastronomia, Istituto Nazionale di Astrofisica, Via Piero Gobetti 101, 40129 Bologna, Italy
[b] Jet Propulsion Laboratory, California Institute of Technology, 4800 Oak Grove Dr., Pasadena, CA 91009, USA
[c] Department of Physics and Astronomy, The University of Iowa, 203 Van Allen Hall, Iowa City, IA 52242-1479, USA
[d] Istituto di Astrofisica e Planetologia Spaziali, Istituto Nazionale di Astrofisica, Via del Fosso del Cavaliere 100, 00133 Rome, Italy
[e] Institut de Planetologie et d'Astrophysique de Grenoble, Bâtiment D de physique - BP 53, 38041 Grenoble Cédex 9, France
[f] Space Research Centre of the Polish Academy of Sciences, ul. Bartycka 18A, Warsaw, Poland
[g] Dipartimento di Ingegneria dell'Informazione, Elettronica e Telecomunicazioni, Università di Roma "La Sapienza", Via Eudossiana 18, 00184 Rome, Italy
[h] Center for Earth and Planetary Studies, National Air and Space Museum, MRC 315, Smithsonian Institution, PO Box 37012, Washington, DC 20013-7012, USA

ARTICLE INFO

Article history:
Received 9 June 2014
Accepted 23 July 2014
Available online 1 September 2014

Keywords:
Mars Express
Mars
Ground Penetrating Radar (GPR)
Ionosphere
Ice
Water

ABSTRACT

Mars Express, the first European interplanetary mission, carries the Mars Advanced Radar for Subsurface and Ionosphere Sounding (MARSIS) to search for ice and water in the Martian subsurface. Developed by an Italian–US team, MARSIS transmits low-frequency, wide-band radio pulses penetrating below the surface and reflected by dielectric discontinuities linked to structural or compositional changes. MARSIS is also a topside ionosphere sounder, transmitting a burst of short, narrow-band pulses at different frequencies that are reflected by plasma with varying densities at different altitudes. The radar operates since July 2005, after the successful deployment of its 40 m antenna, acquiring data at altitudes lower than 1200 km. Subsurface sounding (SS) data are processed on board by stacking together a batch of echoes acquired at the same frequency. On ground, SS data are further processed by correlating the received echo with the transmitted waveform and compensating de-focusing caused by the dispersive ionosphere. Ground processing of active ionospheric sounding (AIS) data consists in the reconstruction of the electron density profile as a function of altitude. MARSIS observed the internal structure of Planum Boreum outlining the Basal Unit, an icy deposit lying beneath the North Polar Layered Deposits thought to have formed in an epoch in which climate was markedly different from the current one. The total volume of ice in polar layered deposits could be estimated, and parts of the Southern residual ice cap were revealed to consist of $\approx$10 m of CO_2 ice. Radar properties of the Vastitas Borealis Formation point to the presence of large quantities of ice buried beneath the surface. Observations of the ionosphere revealed the complex interplay between plasma, crustal magnetic field and solar wind, contributing to space weather studies at Mars. The presence of three-dimensional plasma structures in the ionosphere was revealed for the first time. MARSIS could successfully operate at Phobos, becoming the first instrument of its kind to observe an asteroid-like body. The main goal pursued by MARSIS, the search for liquid water beneath the surface, remains elusive. However, because of the many factors affecting detection and of the difficulties in identifying water in radar echoes, a definitive conclusion on its presence cannot yet be drawn.

1. Introduction

Mars is today a cold, dry and sterile world with a thin atmosphere made of CO_2. The geologic and compositional record of the surface reveals however that in the past Mars had a thicker atmosphere and liquid water flowing on its surface. For this reason, it has been postulated that life could have developed and that some primitive life forms may be existing even today. This possibility has led to the growth of an enormous interest in the red planet, and its exploration now involves all major space agencies in the world. Mars Express, the first European interplanetary mission, was designed to provide unprecedented global coverage

* Corresponding author. Tel.: +39 051 6399 541.
E-mail address: roberto.orosei@inaf.it (R. Orosei).

http://dx.doi.org/10.1016/j.pss.2014.07.010
0032-0633/

of the planet's surface, subsurface and atmosphere, focusing on two related issues: the current inventory of ice or liquid water in the Martian crust, and possible traces of past or present biological activity on the planet (Chicarro et al., 2004).

Mars Advanced Radar for Subsurface and Ionosphere Sounding (MARSIS) was included in the Mars Express payload to search for ice and water in the Martian subsurface. Developed by a team of Italian and US researchers and industrial partners, MARSIS works by transmitting low-frequency, wide-band radio pulses that are capable of penetrating below the surface and are reflected by dielectric discontinuities linked to structural or compositional changes. MARSIS is also capable of operating as a topside ionosphere sounder, transmitting a burst of short, narrow-band pulses at different frequencies that are reflected by plasma with varying densities at different altitudes (Picardi et al., 2004b).

The first instrument of its kind to fly since the ALSE experiment on-board Apollo 17 (Porcello et al., 1974), MARSIS started acquiring scientific data in June 2005, after the successful deployment of its 40-m antenna. Since then, it has produced more than 100 GBytes of data over thousands of orbits, each consisting of several hundred observations. In the following sections, instrument and data characteristics will be summarized, and main scientific results obtained over a nine year period will be presented.

2. The instrument

The Mars Advanced Radar for Subsurface and Ionospheric Sounding (MARSIS) on the Mars Express spacecraft operates from a highly elliptical orbit with a periapsis altitude of 250 km but acquires data only from altitudes lower than 1200 km. This radar has been successfully operating since August 2005. The subsurface sounder is a dual channel low-frequency radar operating between 1.3 and 5.5 MHz with wavelengths between 230 and 55 m in free space for subsurface sounding and between 0.1 and 5.5 MHz (wavelengths between 3000 and 55 m) for ionospheric sounding. The subsurface sounder can operate at one or two-frequency bands out of four available bands. The subsurface sounding radar transmits radio frequency (RF) pulses of 250 μs duration through a 40 m dipole antenna. The return echoes are then converted to digital form and temporarily stored on board for some digital processing. This processing reduces the data rate produced by the instrument to rates allowed by the spacecraft communications channel. These processed returns are then sent to Earth by the telecommunications system on the spacecraft. Advances in digital data acquisition and processing since 1972 have enabled this technique to be used in a compact spacecraft science instrument. This sounder has obtained returns from several kilometres below the surface of Mars. The ionospheric sounder operates at altitudes greater than 800 km in a mode that sweeps the entire 0.1–5.5 MHz range. During ionospheric sounding, the transmitter sends a 91 μs tone at 127 pulses per second rate. The frequency sweep takes 7.3 s to complete the 0.1–5.5 MHz range.

The ionospheric and subsurface sounders share much of the MARSIS hardware. The ionospheric sounder uses a simple low bandwidth pulse and radiates through the dipole antenna. The subsurface sounder operates over four possible frequency bands of 1 MHz bandwidth each using a 250 μs frequency swept transmit pulse. The subsurface sounding channel includes a transmitter and receiver which share the 40 m tip to tip dipole antenna. In sites with a rough surface, the subsurface dynamic range is strongly reduced by echoes received from surface clutter. Off-nadir echoes from areas extending in the along-track direction are reduced by the synthetic antenna processing.

The basic block diagram of MARSIS is shown in Fig. 1. MARSIS consists of (1) a sounder channel containing a programmable signal generator, a transmitter that drives a 40 m dipole antenna and a receiver with an analogue-to-digital converter; (2) a surface cancellation channel consisting a 7 m monopole antenna and a receiver with an analogue-to-digital converter; (3) a dual channel data processor; and (4) a digital electronics and power and control subsystem that controls all the sounder.

The MARSIS subsurface sounding modes operate at altitudes lower than 900 km. The MARSIS transmitter generates a swept frequency high-power RF pulse that is delivered to the antenna for radiation. This radiated energy is reflected from the Martian surface and subsurface back to the radar. Data processing is performed on board in the MARSIS instrument. MARSIS' principal operational parameters of the subsurface sounder are outlined in Table 1. MARSIS utilizes the technique of Doppler beam sharpening (DBS) in order to enhance the ratio of subsurface echoes to surface clutter.

To acquire data with a sufficient signal-to-noise ratio, MARSIS employs a 1 MHz bandwidth linearly swept signal for transmission in the subsurface sounding modes. This waveform has a duration of 250 microseconds duration. During on-board or ground data processing, the return signal is range compressed, increasing the signal-to-noise ratio by about 24 dB. The MARSIS electronics control of pulse compression side-lobes was an overriding issue. The expected return of the first specular signal was calculated to be very strong compared to the calculated subsurface reflections. In order to prevent the subsurface return from being masked by the side-lobes of the specular first surface reflection, the side-lobe levels were required to be very low. The required impulse response of the system, after passing the received signal through a Hanning weighting function, is for all side-lobes to be below a time-dependent level specified by the solid line in Fig. 2.

2.1. Antenna

The 40-m tip-to-tip dipole consists of two 20 m elements. Each element consists of a fibreglass tube with wire attached inside to act as the antenna conductor. The elements are folded individually and stowed in a rectangular carrier for launch. After arrival at Mars, a pyrotechnic device released the elements one at a time, at right angles to the spacecraft solar array.

The 7-m monopole has similar construction to the dipole elements, but is smaller diameter and deployed at a right angle to the dipole parallel to the spacecraft Z axis.

2.2. Radar sensor electronics

The electronics assembly consists of two boxes. The first contains the digital electronics subsystem (DES) and receiver assembly, while the second box contains the transmitters and interfaces to the antenna. Both these boxes are housed inside the Mars Express structure, while the antenna box is located on the outside of the spacecraft. The monopole antenna contains a pre-amplifier at the mounting plate of the structure.

2.3. Transmitter

The transmitter assembly controls the signal flow between the antenna and the receiver electronics. The transmitter control signals are generated in the DES. The low level swept frequency pulse from the signal generator is amplified and routed into a wideband matching network. The matching network allows multi-frequency operation on a pulse-to-pulse basis with no switching, so operational modes can be designed with any desired combination of frequencies bands between 1.3 and 5.5 MHz.

A transmit/receive (T/R) switch is located between the transmitter output and the matching network input. The T/R switch

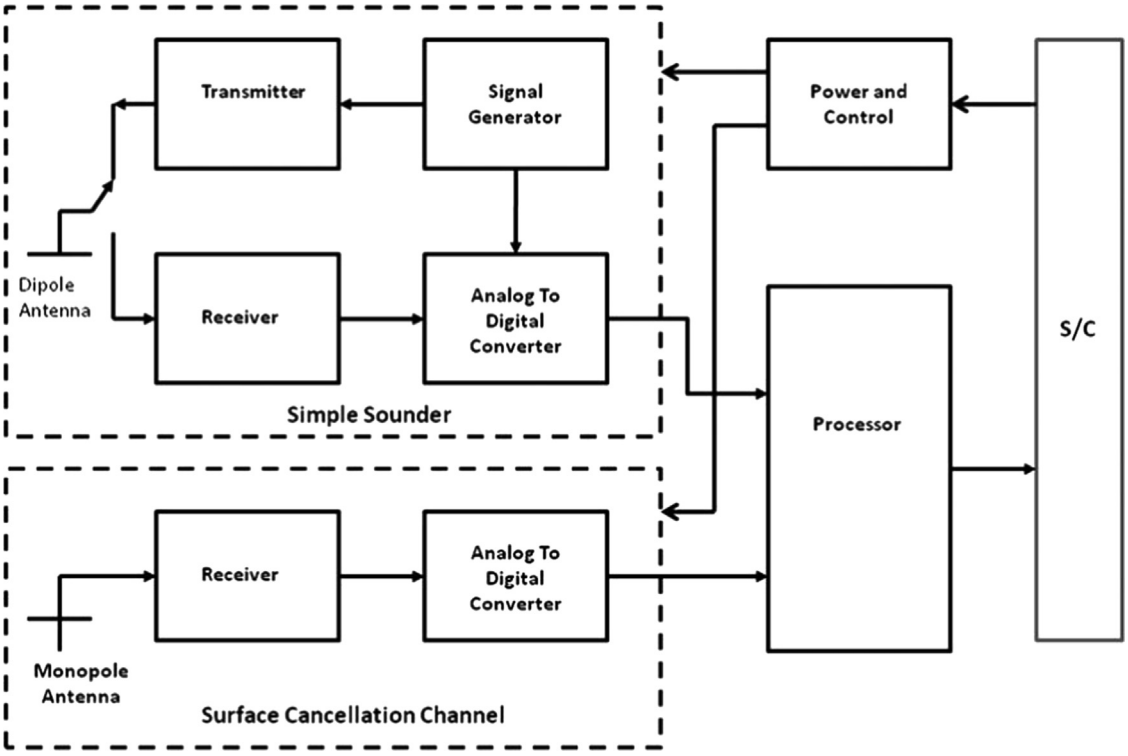

Fig. 1. Conceptual block diagram of MARSIS.

Table 1
MARSIS subsurface sounder parameters.

Parameter	Description
Subsurface sounding altitude range	250–900 km
Antenna length	40 m tip-to-tip
Subsurface sounder frequency range	1.3–5.5 MHz in 4 bands
Peak radiated power	1.5–5 W
Subsurface sounder pulse repetition rate	127 Hz
Subsurface sounder transmit pulse length	250 microseconds
Subsurface sounder wavelength	60–160 m
Bandwidth per band	1 MHz
Sounder free space depth resolution	150 m
Sounder dynamic range	40–50 dB
Nominal window depth	15 km
Number of processed channels	2 or 4
Number of simultaneous frequencies	1 or 2
Data quantization	8 bits per sample
Data quantization rate	2.8 megasamples per second
Data window duration	350 microseconds
Data rate output	18 to 75 Kilobits per second
Data volume	285 Megabits per day
DC operation power	60 W
Total mass	20 kg

protects the receiver from high voltages during transmit pulses and isolates the transmitter during receive to reduce signal loading. For the ionospheric sounding mode, the wideband antenna matching network is bypassed and the antenna is coupled to the transmitter with a transformer. The transformer allows a high voltage to be placed on the antenna over a wide frequency range without the size and mass cost of a matching network.

2.4. Receiver

The radio frequency electronics receiver resides in the DES housing. It consists of the chirp/local oscillator distributor and the dual channel receiver radio frequency subsystem-receive electronics (RFS-RX), which down converts and amplifies the returns

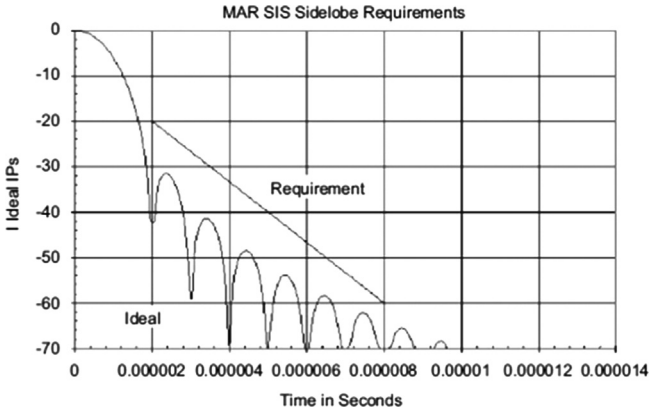

Fig. 2. Diagram illustrating the ideal impulse response of the system and the requirement on side-lobe level, to prevent the subsurface return from being masked by the side-lobes of the specular first surface reflection.

from the dipole and monopole antennas. The receiver is composed of a power divider, switches, amplifiers, mixers, bandpass filter banks, and low-pass filters, which provide for two receive channels.

Following RF amplification and filtering, the received signal is down converted and then low pass filtered, amplified and gain controlled. The received signals are then converted to digital form by two 8-bit analogue-to-digital converters, one in each receiver channel. After buffering, the digital receive signals are routed to the digital electronics.

2.5. Digital electronics

The command and control of the instrument resides in the Digital Electronics Subsystem (DES).

The MARSIS subsurface sounder has five basic operating modes for subsurface sounding and one additional mode for ionospheric sounding. Each mode sets the number of frequencies that may

operate, the use of the clutter cancellation channel (the monopole channel), if required, the use of pre-summing, and the number of Doppler filters that will be downlinked. The five subsurface sounding modes (SS1–SS5) are

SS1: 2 frequency bands/2 antennas/1 Doppler filter.

SS2: 2 frequency bands/1 antenna (dipole)/on-board multi-look. This mode carries out on board non-coherent integration of five looks and downloads a single amplitude detected averaged echo profile for each synthetic aperture (frame), at two-frequency channels.

SS3: 2 frequency bands/1 antenna/3 Doppler filters. This mode allows downlink, for each frame, of the I/Q data of three Doppler filters collected on the dipole antenna channel at two frequencies. Range processing is performed on the ground.

SS4: 1 frequency band/2 antennas/5 Doppler filters. This mode allows downlink, for each frame, of the I and Q data of five Doppler filters (around the zero Doppler filter) for both the dipole and the monopole channels at one frequency. Range processing is performed on the ground. In this mode it is possible to perform, on the ground, the dual antenna cross-track clutter cancellation with a five look non-coherent integration on each frame.

SS5: 1 frequency band/2 antennas/short pulse (30 μs)/3 Doppler filters. This mode uses a short-pulse waveform to reduce the impact of uncontrolled side-lobes on deep subsurface reflections. The echoes returning after the transmission of four short pulses with the same carrier frequency are pre-summed upon reception, and the I/Q processed data at two antennas and three Doppler filters are downlinked for each frame. Range compression and clutter cancellation are performed on the ground.

AIS: Active ionospheric sounding. This is the active sounding mode used when the spacecraft is at an altitude higher than 900 km or when no SS mode is being used (Table 2). In AIS mode MARSIS is used as a topside ionosonde to probe the Martian ionosphere by detecting reflections from layers of differing electron density. During AIS mode, a 91.4 μs transmit pulse is generated at a single frequency, and the receive window is opened as soon as possible after the pulse to energy at that frequency only. The system then steps to the next frequency at a 127 Hz rate and repeats until each of the 160 frequencies in the table have been sampled to form a single ionogram. One ionogram is generated every 7.543 s.

2.6. Data characteristics

In Subsurface Sounding (SS) mode, MARSIS transmits a 250 μs linearly modulated pulse "chirp" receiving its echo before transmitting a new one. Echoes are collected in groups called "frames", and then processed together on board. Frames contain a variable number of pulses, as a function of altitude and frequency. Dual-frequency modes (see previous section) transmit two closely spaced pulses at different frequencies receiving their echoes separately (Jordan et al., 2009). On-board processing consists in stacking together all echoes at the same frequency within a frame after compensating for the vertical motion of the spacecraft. This technique, called Doppler-beam sharpening, can be used to compensate the spacecraft motion in directions that are different from the vertical one. The result of stacking echoes after motion compensation is called a Doppler filter, and different SS modes produce a variable number of them, usually pointing at nadir or in directions close to nadir (Jordan et al., 2009). Further processing is required on ground, as the transmitted waveform is much longer than the required range resolution of 150 m in free space, corresponding to 1 μs in pulse width. Thus, MARSIS SS data are completely unintelligible before ground processing.

The Active Ionospheric Sounding (AIS) mode of MARSIS is much simpler than the subsurface mode described above. It is a swept frequency topside sounder, following the basic description of Franklin and Maclean (1969). Examples of ground-breaking topside sounders are the ISIS and Alouette series (see Benson and Bilitza, 2009). For reviews of the design and history of this kind of sounder, see Franklin and Maclean (1969) and Benson (2010). In a swept frequency sounder, the sounder sends out an intense radio signal, or "sounding pulse," at a pre-set frequency, and then "listens" for a reply. After a specified listening interval, the transmission frequency is incremented and another sounding pulse is sent, with another listening interval. The array of intensities as a function of sounding frequency and delay time is called an ionogram. This is the basic unit of data output for a swept frequency sounder.

In Fig. 3 from Morgan et al. (2008) we show an ionogram, with sounding frequency on the horizontal axis and delay time on the left-hand vertical axis. The right-hand vertical axis shows apparent range, computed as $r_{app} = (c/2)T_{delay}$, which is the calculated distance from the spacecraft assuming the absence of dispersion due to plasma. On this ionogram, we show the ionospheric trace along with several other data objects that are available from an ionogram: the electron plasma frequency harmonics, which give the local electron density; the electron cyclotron echoes, which give the local magnetic field strength; and the planetary surface

Table 2
MARSIS ionospheric sounder parameters.

Parameter	Value
Ionospheric sounding altitude range	≈1200–250 km
Ionospheric sounder frequency range	100–5.5 MHz
Discrete frequencies used for sounding	160
Ionospheric sounder transmit pulse length	91.4 μs
Ionospheric sounder pulse repetition rate	127 Hz
Receive window after pulse	254–7566 μs
Ionogram frame length	1.26 s
Ionogram frame interval	7.543 s
Detection bandwidth	10 kHz

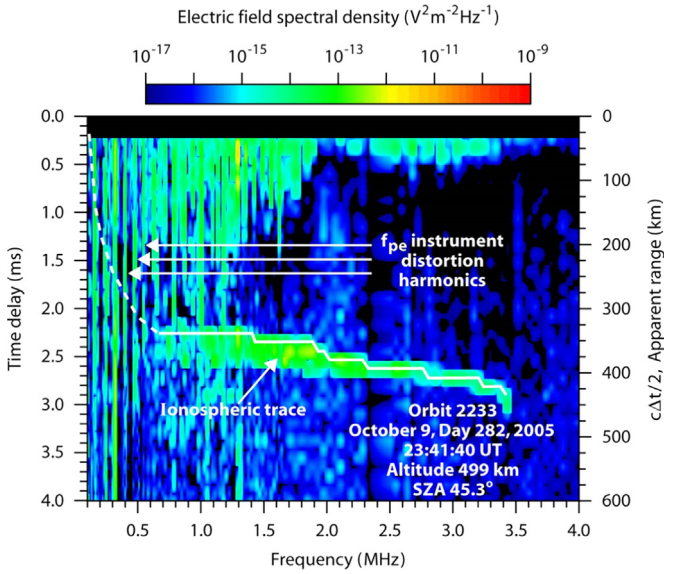

Fig. 3. A sample ionogram (from Morgan et al., 2008).

reflection, which can be used as a measure of ionospheric attenuation of the sounding wave, an indicator of excess electron density in the ionosphere.

2.7. Ground data processing

In SS mode, MARSIS transmits a modulated waveform to achieve a range resolution equal to the inverse of the transmitted bandwidth, after processing on ground (Jordan et al., 2009). Such processing is called range compression, and consists in the correlation between the received echo and the transmitted waveform. This achieves the desired resolution and increases significantly the signal to noise ratio (SNR), but produces also side-lobes, artefacts that may mask secondary echoes coming after the surface reflection unless further filtering of the signal is applied (see Fig. 2). Data that have been processed this way are usually displayed as radargrams, that is grey-scale images in which the horizontal dimension corresponds to distance along the ground track, the vertical dimension is the round trip time of the echo, and the brightness of the pixel is the logarithm of echo strength.

The radargram for orbit 5017 shown in Fig. 4 reveals also one of the main problems affecting MARSIS data, that is ionospheric defocusing. Plasma in the ionosphere of Mars acts as a dispersive medium for electromagnetic waves, having a frequency-dependent index of refraction. MARSIS operates in the MHz range, and typical values for maximum plasma frequency in the Martian ionosphere are of a few MHz. With a frequency close to the maximum plasma frequency and a large fractional bandwidth, pulses transmitted by MARSIS can be severely distorted as waves at different frequencies within the bandwidth of the signal propagate at different velocities. The effect on the received echo is a degradation of the signal to noise ratio and a loss of range resolution due to the broadening of the pulse. Especially at times of strong solar activity, these effects can be so strong that they make radar data unintelligible. Over the years since the start of the development of MARSIS, several methods were developed to correct this distortion, such as those by Safaeinili et al. (2003), Ilyushin and Kunitsyn (2004), Mouginot et al. (2008), Zhang et al. (2009) and Cartacci et al. (2013). They are all based on the maximization of a function of the signal through the differential variation of the phase of the components of the Fourier signal spectrum. The algorithm used in producing publicly-available data is called contrast method (Cartacci et al., 2013).

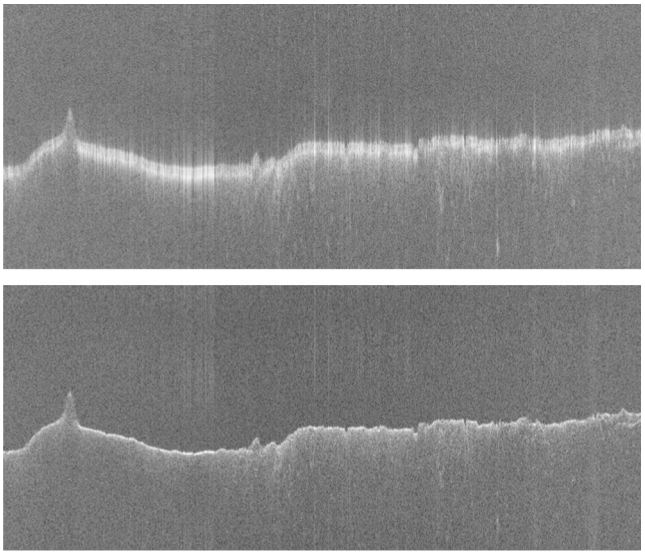

Fig. 4. Radargram for orbit 5017 before (top) and after (bottom) the use of the contrast method (Cartacci et al., 2013) to correct ionospheric distortion.

The antenna of MARSIS has negligible directivity, with the consequence that the radar pulse illuminates the entire surface beneath the spacecraft and not only the near-nadir portion from which subsurface echoes are expected. If the surface of the body being sounded is not smooth, then part of the incident radiation is scattered in directions different from the specular one. Areas that are not directly beneath the radar can scatter part of the incident radiation back towards it, and thus produce surface echoes reaching the radar after the echo coming from nadir. This can mask, or be mistaken for, subsurface echoes. This surface backscattering from off-nadir directions is called “clutter”.

Clutter can produce in a radargram the impression of subsurface structures where there are in fact only off-nadir surface echoes. For this reason, the detection of subsurface interfaces is usually validated through numerical electromagnetic models of surface scattering, such as those by Nouvel et al. (2004). Such models are used to produce simulations of surface echoes, which are then compared to real echoes detected by the radar (see Fig. 5 for an example). If a feature appears both in the radargram and in the simulation, then it is concluded that such feature is a lateral surface echo and not a subsurface reflection.

Ground processing of AIS data consists in the reconstruction of the electron density profile as a function of real (as opposed to apparent) altitude. The ionospheric trace shown in Fig. 3 is the reflection of the sounding wave from the ionosphere. Because the index of refraction of a radio wave in a plasma (neglecting the existence of magnetic fields) is given by

$$n = [1 - (f_p/f_s)^2]^{1/2} \quad (1)$$

implying that the group velocity is given by

$$v_{group} = c[1 - (fp/fs)^2]^{1/2} \quad (2)$$

the wave cannot propagate and therefore must be reflected when the plasma frequency becomes equal to the frequency of the sounding wave. This allows the swept frequency of the radar sounder to be a probe of the electron density of the ionosphere. The trace is essentially a plot of the apparent altitude against the sounding frequency or plasma frequency in the ionosphere. Because the wave is travelling through a plasma medium, the apparent altitude must be corrected for dispersion. How this has been done for the MARSIS AIS data is described by Morgan et al. (2008), Morgan et al. (2013b), and Morgan et al. (2014). This procedure is based on time-tested methods described by Budden (1961), Jackson (1969), Rishbeth and Garriott (1969), Zou and Nielsen (2004) and a host of others. The method used for “inversion” of an ionospheric trace is described by these authors and others as the “lamination” method, meaning that the dispersion is accounted for in the top layer of the ionosphere below the spacecraft, and that this result is used to solve for the next layer. The top two layers are then accounted for, allowing the solution for the third layer, and so on, until all the layers are solved.

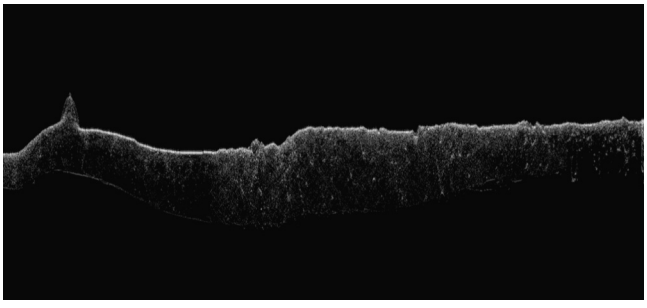

Fig. 5. Simulated radargram for orbit 5017. Comparison with Fig. 4 reveals a potential subsurface echo in the rightmost part of the radargram.

One should notice that the lamination method requires that the electron density at the spacecraft be known. In fact, the artefact labelled "plasma frequency harmonics" in Fig. 3 in many cases provides the local electron density at the spacecraft. This quantity has, through the history of MARSIS, been collected manually with the aid of a cursor-driven adjustable scale on the computer monitor used to display an ionogram; however, automated methods of taking these data have now been developed and will soon supercede the manual method (see Andrews et al., 2013). The process of getting local electron density from the plasma frequency harmonics is discussed by Gurnett et al. (2005), Gurnett et al. (2008), Duru et al. (2008), Morgan et al. (2008), and Morgan et al. (2013a). The origin of the plasma frequency harmonics as an artefact of feedback from the sounding pulse that is then clipped in the pre-amp – receiver complex, is discussed in the last named reference.

The local densities derived from the plasma frequency harmonics are an interesting and valuable data set even without their supporting role in inversion of the ionospheric trace. Results from analysis of these data will be presented in a later section of this paper.

The electron cyclotron echoes shown in Fig. 3 are the result of the acceleration of electrons by the initial increase in electric field on the antenna as a result of the sounding pulse. In the presence of an electric field, these electrons are accelerated perpendicular to their direction of motion, causing them to execute circular or helical motion with the electron cyclotron frequency. They therefore impact the antenna at the cyclotron frequency, causing intense and sharply defined signals spaced at the electron cyclotron period. This phenomenon is illustrated in Fig. 3.

The MARSIS AIS electron cyclotron echoes and the extraction of the magnetic field strength was first discussed by Gurnett et al. (2005) and again by Gurnett et al. (2008). The electron echoes and the resulting magnetic field strengths were first used en masse by Akalin et al. (2010) to map the field strength as a function of altitude and solar zenith angle. The data are taken manually using an adjustable scale on a computer monitor with the visual ionogram displayed, exactly the same as with the plasma frequency harmonics. As with the plasma frequency harmonics, automated methods are under development that will certainly retire the manual method.

Unlike the plasma frequency harmonics, the electron cyclotron echoes have no role in processing the electron density profiles; however, like the plasma frequency harmonics, they constitute a valuable data set on their own. We shall discuss how these data have been used to further knowledge of the Martian ionosphere in a later section of this paper.

Use of attenuation of the planetary surface reflection as an indicator of increased electron density due to impinging energetic particles is discussed by Morgan et al. (2006) and Morgan et al. (2010).

3. Main results of subsurface sounding

3.1. Planum boreum

After the deployment of its antenna, which took place in June 2005, the first observations of MARSIS were acquired over Planum Boreum, a large geologic feature more than 1000 km across covering the North polar region of Mars, and composed mostly of water ice with a few percent of dust (Byrne, 2009). Planum Boreum consists of different geologic units: the Northern residual ice cap (NRIC), the North polar layered deposits (NPLD) and the basal unit (BU). The NRIC is a high albedo feature predominantly composed of H_2O ice (Langevin et al., 2005) and is commonly interpreted as the current site of NPLD formation (Byrne, 2009). The NRIC is superimposed on the NPLD, which consists of stacks of finely layered dusty water ice more than 2 km thick, and whose stratification is thought to be the result of climatic variations over timescales of 10^5–10^9 years (e.g. Byrne, 2009). The BU lies below the NPLD, appears to have a much higher content of dust, and is thought to have formed in an epoch in which climate was markedly different from the current one (Byrne and Murray, 2002).

In an early MARSIS orbit, 1855, the NPLD were observed in the frequency bands centred at 3.0 and 5.0 MHz (Picardi et al., 2005) (Fig. 6). The time delay to and the relative echo strength of the basal reflector were found to be consistent with the NPLD material having a dielectric constant and loss tangent similar to that of fairly pure water ice, while the characteristics of the echoes were not compatible with the presence of a melt zone at the base of the NPLD. The lack of a flexural/membrane downward deflection of the plains beneath the NPLD (after correcting for the velocity of propagation within the NPLD) was interpreted as requiring a very thick elastic lithosphere and a low crust/upper mantle temperature gradient.

The acquisition of subsequent observations over Planum Boreum allowed a study of its internal structure (Selvans et al., 2010). It was possible to discern the NPLD from the BU, and to map the thickness and extent of these two units. Water ice volume was estimated to be $(7.8 \pm 1.2) \times 10^5$ km^3 in the NPLD, and $(4.5 \pm 1.0) \times 10^5$ km^3 in the BU. No lithospheric deflection was apparent anywhere under Planum Boreum, suggesting that a thick elastic lithosphere has existed at the north pole of Mars since before the emplacement of the BU. A problematic area for mapping the BU extent and thickness was found in the distal portion of the 290°E–300°E region, where MARSIS data showed no subsurface reflectors, even though the BU was inferred to be present from other lines of evidence.

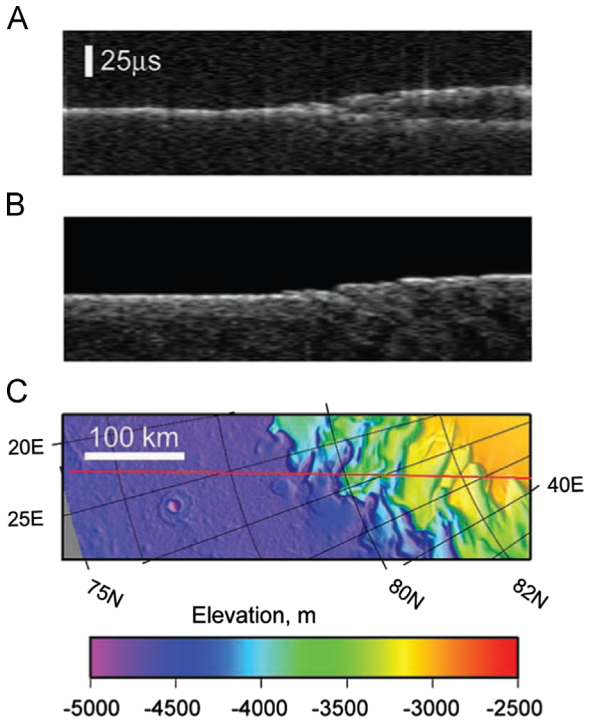

Fig. 6. (A) MARSIS data in radargram format for orbit 1855 as it crosses the margin of the north polar layered deposits. (B) Simulated MARSIS data if echoes are only from the surface (nadir and off-nadir clutter). (C) MOLA topography along the ground track (red line); elevation is relative to the mean planetary radius. MARSIS data at 5 MHz show a split of the strong return into two as the ground track reaches the NPLD (higher terrain to the right). Maximum time delay to the second reflector is 21 μs, equivalent to 1.8 km depth in water ice (from Picardi et al., 2005). (For interpretation of the references to color in this figure caption, the reader is referred to the web version of this article.)

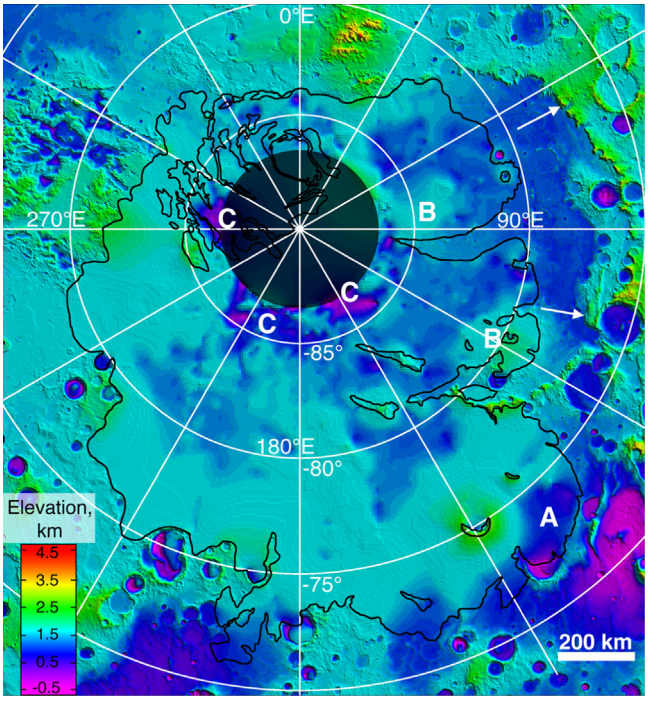

Fig. 7. Topography of the south polar region of Mars from MGS MOLA data. The SPLD unit mapped by Tanaka and Kolb (2005) is outlined in black, with topography at the SPLD basal interface shown, based on MARSIS measurements of SPLD thickness. A indicates a depression below a distal SPLD lobe. B indicates relative highs within the remnant Prometheus basin (basin rim indicated with arrows). C indicates depressions in the near-polar region (from Plaut et al., 2007b).

Between June and December 2011, MARSIS collected over 250 high quality observations of the NPLD. During the prime period of the campaign, the periapsis of the Mars Express orbit passed over the north polar plateau on the night side. This combination of low altitude and night side produced the highest resolution along-track (<5 km) and the best signal-to-noise due to the absence of ionospheric distortion and absorption. The higher quality of the data allowed the mapping of the BU over the entire extent of Planum Boreum. Weak echoes within the BU outlined a two-layer structure, perhaps corresponding to the Rupes Tenuis unit and the Planum Boreum Cavi unit identified by Tanaka et al. (2008) within the BU (Frigeri et al., 2012). The echo time delay between the surface return and the lower contact of the BU was used to derive a real relative dielectric constant of approximately 4 for its material, significantly higher than that of pure water ice, or of the NPLD alone observed at Gemina Lingula (Picardi et al., 2005). This value requires a fraction of dust that, for a mafic component, could be as high as 50% (Plaut et al., 2012).

3.2. *Planum australe*

Similar to Planum Boreum, Planum Australe is an ice-rich cap extending across the southern polar region of Mars. It consists of three main units, a Southern residual ice cap (SRIC), the South polar layered deposits (SPLD) and the Dorsa Argentea Formation (DAF). The SRIC is composed of high-albedo solid CO_2 and it is estimated to be on the order of a few meters thick (Byrne, 2009), while the SPLD are similar in structure to the NPLD. The DAF extends around the SPLD, appearing as a relatively smooth plain crossed by sinuous ridges, and is thought to be the devolatilized remnant of an ancient polar ice sheet (Byrne, 2009).

The SPLD were extensively observed by MARSIS to produce a map of their thickness and extent (Plaut et al., 2007b). The interface between the SPLD and the underlying lithic substrate was detected beneath most of the SPLD, although in places it was found to be discontinuous, indistinct or absent. Sometimes, however, basal echoes appeared equivalent to or brighter than the surface echo, which is not expected for propagation through a lossy medium. An extended area of unexpectedly bright basal reflections was found in an area between the thickest part of the SPLD (≈ 3.7 km) and the nearby SPLD margin, from 310° to 0°E. While a strong contrast in dielectric constant at the base may be responsible, it is deemed highly unlikely that liquid water (basal melting) caused the bright return, because it occurs below thin (as well as thick) sections of the SPLD that are among the coldest places on the surface of Mars.

The map of the sub-SPLD topography is typically low in relief, with broad areas of higher and lower topography. A pronounced low area is seen near the SPLD margin around 72°–74°S, 130°–145°E, and elevated regions within the remnant Prometheus impact basin are seen to continue below the SPLD at 78°–82°S, 100°–130°E and from 70°–90°E poleward of about 83°S. An unexpected feature of the basal topography is a series of depressions at the highest latitudes (84°–87°S). These occur discontinuously from longitudes 95° to 295°E. The depressions range in width from 50 to 200 km, and reach a depth of as much as 1 km below the surrounding sub-SPLD topography. On a regional scale, the basal interface is relatively flat. The lack of evidence of regional down-warping in response to the SPLD load suggests that the elastic lithosphere in the south polar region is very thick (>150 km), as was inferred for the north polar region.

A thickness map of the SPLD was generated by subtracting the elevations of the interpolated basal topography from the high-resolution MOLA surface topography (Fig. 8). The distribution of SPLD thickness reflects the asymmetry of the south polar geology, with the thickest portions offset from the pole near 0°E, and the much more areally extensive but thinner portion centred near 180°E. The newly discovered near-polar depressions showed clearly as anomalously thick areas, as did several of the distal lobes. The maximum measured thickness was 3.7 ± 0.4 km, under the highest elevations of the SPLD near 0°E. The integrated volume of the entire SPLD is estimated at $1.6 \pm 0.2 \times 10^6$ km^3. This translates to an equivalent global water layer thickness of 11 ± 1.4 m (assuming an SPLD composition of nearly pure ice), and is within the range estimated by previous workers using MOLA data alone (Smith et al., 2001).

A dedicated search for very strong subsurface reflections from the base of the SPLD was performed by Cartacci et al. (2008), who found other areas beyond what presented in Plaut et al. (2007b) where basal echoes are stronger than surface echoes. An analysis of known surface properties did not provide an explanation of the occurrence of such bright basal echoes. However, simple simulations of electromagnetic propagation could reproduce the observed behavior if the areas of bright subsurface reflections are overlaid by a 10–100 m thick layer of CO_2 ice, with or without a thin coating of dust. These results hinted at the possibility that MARSIS could be used to map the presence of CO_2 ice over the SPLD, even when such ice is covered by dust.

Plaut et al. (2007a) found that subsurface interfaces exist beyond the margins of the SPLD, to depths that, depending on the material that is hypothesized to constitute the upper layer, range from 600 m to 900 m. These interfaces are found over a wide area of the south polar region on approximately 2/3 of periphery of the SPLD, as far as 1000 km beyond their margin. Their spatial distribution correlates very well with the Hesperian Dorsa Argentea Formation as mapped by Tanaka and Scott (1987). This fact leads to the inference that the material constituting the DAF is markedly different from that of surrounding geologic units outside the SPLD, perhaps because of a substantial ice content.

The portion of the DAF including Chasma Australe was further investigated by Farrell et al. (2008), finding that the radar layer

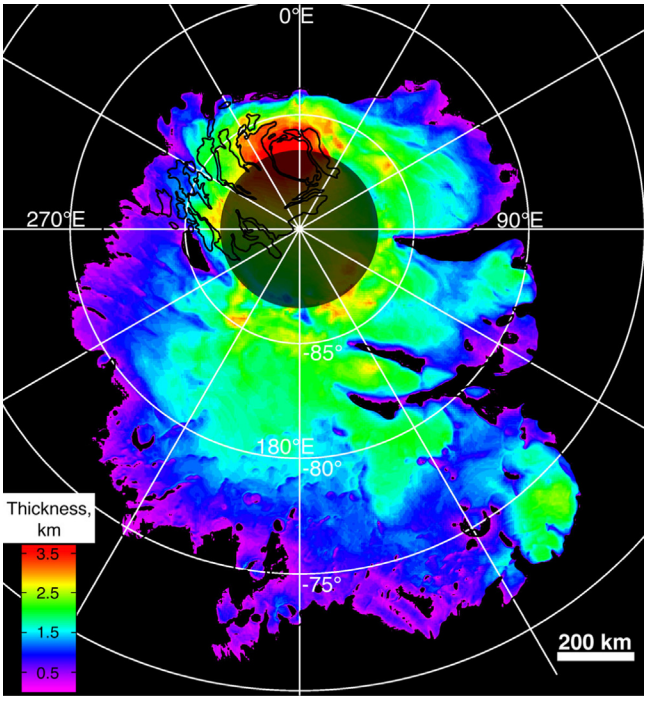

Fig. 8. Map of the SPLD thickness, based on MARSIS measurements and MOLA surface topography. An anomalous thick section appears in lower right (see A in Fig. 7). The thickest areas occur beneath the highest elevations of the SPLD (red areas near top), and in association with the near-polar depressions (see C in Fig. 7) (from Plaut et al., 2007b). (For interpretation of the references to color in this figure caption, the reader is referred to the web version of this article.)

correlated with the DAF continued beneath the SPLD, and that its disappearance a few hundred km into the SPLD might be due to absorption of the signal by the SPLD itself rather than by its end. A fluvial origin for Chasma Australe or the existence of a paleolake at its head were ruled out by the characteristics of radar data. Strata-like linear features within the SPLD were noted by both Plaut et al. (2007b) and Farrell et al. (2008), but their interpretation in terms of reflections from distinct and sharp ice-ice interfaces of varying impurity content is countered by the finding that, in some places, the depth of the layers changes when examining two different MARSIS frequency bands.

Milkovich et al. (2009) studied the stratigraphy of Promethei Lingula in the SPLD, using both MARSIS and SHARAD (Seu et al., 2007) radar data. It was found that, within this region, reflections detected by MARSIS correlated with layer packets observed in images, while in tenfold higher resolution SHARAD data it could be seen that an individual reflection corresponded to 3–7 layers in images at resolutions of 6 m/pixel. This correspondence allowed the tracing of layers within Promethei Lingula. It was found that layers are not horizontal, but are higher toward the centre of the SPLD and lower toward the margins. Layers generally follow the topography, but in some locations they intersect with the surface, indicating that multiple episodes of significant erosion have occurred in local regions within Promethei Lingula during SPLD history.

A different method to study the upper stratigraphy of the SPLD was developed by Mouginot et al. (2009): using simulations of surface reflections, and correlating variations in the ratio between simulated and real echo strength, they could point to regions of different surface reflectivity. In particular, they found that the Southern residual ice cap is a region of extremely low reflectivity, which could be explained by an optically thin layer of very transparent material causing destructive interference between surface and subsurface reflections. The best fit for an electromagnetic model simulating the such interference of the stratigraphy was obtained for a 10 m thick layer of CO_2 ice overlying a basement of H_2O ice. Variations of reflectivity across the SRIC could be explained in terms of variations of either dielectric properties or thickness of the upper layer. In case of uniform composition, the SRIC has to be thicker towards the edges. The total volume of CO_2 in the SRIC is then estimated to correspond to about 5% of atmospheric surface pressure.

3.3. The Medusae Fossae Formation

The Medusae Fossae Formation (MFF) consists of five outcrops covering an area of about 2.1×10^6 km^2 across the crustal dichotomy boundary between 140° and 240°E. The MFF was initially dated as Amazonian in age (Scott and Tanaka, 1986) and interpreted as a deposit of fine-grained material of perhaps volcanic origin (Tanaka, 2000). According to Mandt et al. (2008) the properties of the MFF material are consistent with those of terrestrial ignimbrites, suggesting an origin by pyroclastic flow. More recently, analysis of high-resolution data has provided evidence that parts of the MFF were formed in the Hesperian (Kerber and Head, 2010). Recent modelling of the areal distribution of tephra using a Mars Global Circulation Model predicts that explosive eruptions from Apollinaris Patera might have been the source of the Medusae Fossae Formation (Kerber et al., 2011).

MARSIS data were used to characterize the thickness and electrical properties of the MFF deposits as a guide to their bulk porosity and/or ice fraction (Watters et al., 2007). The subsurface interfaces revealed by MARSIS (Fig. 9) suggest that MFF materials are deposited on generally planar materials in the northern lowlands and the downward slope of the dichotomy boundary. MARSIS data support estimates of the total volume of MFF material calculated using apparent base-level elevations in the lowlands. These estimates range from 1.4×10^6 km^3 (Lanagan et al., 2001) to 1.9×106 km^3 (Hynek et al., 2003). MARSIS observations provide an opportunity to evaluate the electrical properties of the MFF where the material is deposited on lowlands plains that are exposed nearby. The observed time delays in the MFF deposits correspond to a bulk real dielectric constant ε' of $\approx 2.9 \pm 0.4$, based on the projection of the surrounding plains beneath the material.

The dielectric properties of a material are related to its density and composition. The real part of the dielectric constant is modulated strongly by density. The imaginary component of the dielectric constant ε'' and the loss tangent are strongly influenced by target composition. Radar losses due to attenuation in the deposits were estimated using the method outlined in Porcello et al. (1974). At 4 MHz centre frequency (band 3), we obtain losses of $\approx 0.0048 \pm 0.0024$ dB/m. For ε' of 2.9 and a centre frequency of 4 MHz, these losses correspond to a range in loss tangent of ≈ 0.002–0.006. MARSIS studies of the PLD (Picardi et al., 2005; Plaut et al., 2007b) suggest a value for ε' of about 3, consistent with pure water ice, based on the agreement between the inferred depth of the basal interface and the projection of the surrounding surface. The loss tangent of the PLD is estimated to range from < 0.001 to 0.005. Our analysis suggests a similar real dielectric constant (2.5–3.3) and a comparably low range of loss tangent (0.002–0.006) for the MFF materials. The loss tangents derived for the MFF deposits are below the range measured for terrestrial volcanic materials but are comparable to some low-titanium lunar materials (Carrier et al., 1991).

Thus, our first-order estimates of the dielectric losses span a range that includes some dry, unconsolidated geological materials and mixtures of pure water ice and sediment. There are two plausible interpretations of these observations. The first is that the MFF material is poorly consolidated and composed of non-ice

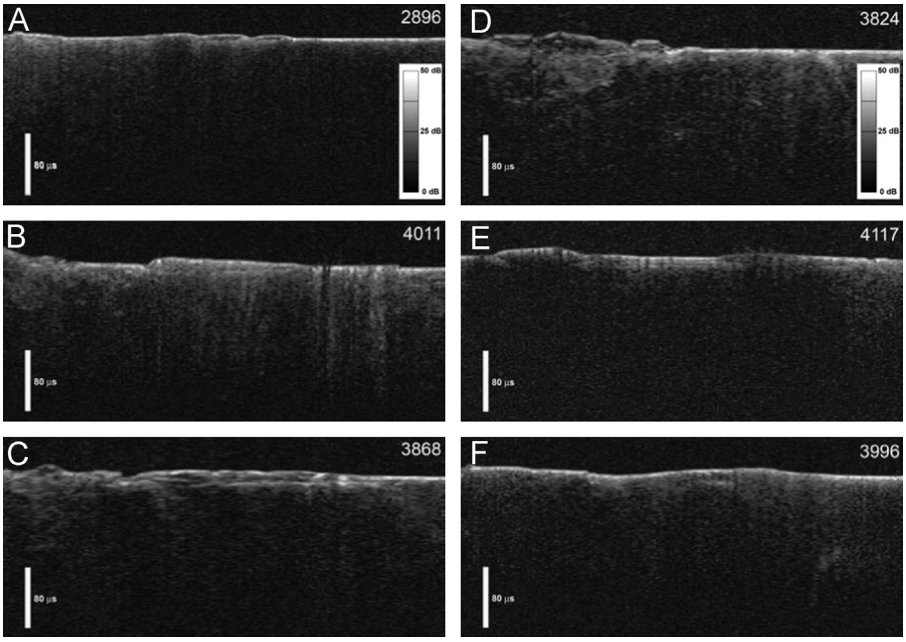

Fig. 9. Radargrams showing MARSIS data for orbit 2896 (a), 4011 (b), 3868 (c), 3824 (d), 4117 (e), and 3996 (f). Echoes are plotted in time delay versus position along the orbit. The subsurface echoes are offset in time delay from the surface echo and are interpreted to be nadir reflections from the interface between the MFF deposits and the lowland plains material. The peak surface return is corrected to agree with the MOLA topography along the orbit track. The radargrams are resampled to a uniform along-track length of $\approx$1000 km. All the orbits are ascending except for orbit 2896 (from Watters et al., 2007).

material with low dielectric loss. If the MFF material is an ice-poor ash or aeolian deposit, it must have an unusually high porosity and low bulk density at depths up to 2.5 km to account for the estimated values of ε'. MFF deposits with a depth-averaged bulk density $>1.9\ \mathrm{g/cm^3}$ will have an ε' value outside the measured range. The second possibility is that the MFF material is ice-rich, with a non-ice component of higher real dielectric constant and loss tangent (ice present as a minor component within a matrix of $\varepsilon'=6$ does not match the observed properties).

3.4. Vastitas borealis

As briefly discussed at the end of Section 3.2, MARSIS echoes can be used to estimate dielectric properties of the Martian surface. Usually, time delay between surface and subsurface echoes is the primary information in reconstructing subsurface stratigraphy, as in the interpretation of radagrams. However, echoes contain also information on the power reflected by the surface, which is tied to its reflectivity and thus to the dielectric permittivity of material from the surface down to a depth of a few tens of meters. Unfortunately, echoes cannot be calibrated through characterization of the transfer function of the instrument, as MARSIS antenna is too large to be tested in controlled conditions on ground.

To circumvent this problem, a calibration method has been developed in Mouginot et al. (2009), using surface scattering simulations such as those described in Nouvel et al. (2004). The method is based on the observation that power reflected by a natural surface depends both on its composition and on its geometry (see Picardi et al., 2004a, for a discussion). If the effect of geometry can be correctly accounted for, through simulations using accurate knowledge of the Martian topography provided by the MOLA altimeter (Smith et al., 2001), then the ratio between measured echo power and the fictitious reflected power estimated through simulations is a function of the unknown gain of the MARSIS antenna and of the Fresnel reflection coefficient of the surface. If an area can be found, in which the surface composition is known, then antenna gain can be estimated, and applied to other measurements to determine the radar reflectivity of the surface.

After the application of this method to the Southern residual ice cap (Mouginot et al., 2009), Mouginot et al. (2010) produced a global map of Martian surface reflectivity, finding that areas of low permittivity concentrate inside the Vastitas Borealis formation, an extensive Hesperian-aged geologic unit covering most of the northern lowlands of Mars. The VBF possesses unique morphologic characteristics, including some of the smoothest surfaces on any planetary body, and its age is similar to that of outflow channels flowing into it. Because of this, Kreslavsky and Head (2002) hypothesize that Vastitas Borealis is a sublimation residue from frozen ponded bodies of water formed by the discharge of outflow channels. As ices in general have a lower dielectric permittivity than rocks, the low permittivity of the VBF is consistent with a high ground ice content and with its origin from the freezing and sublimation of a body of water.

Re-assessing previous results using increased coverage, Mouginot et al. (2012) indeed concluded that the Vastitas Borealis formation has a low dielectric constant compared with that of typical volcanic materials (see Fig. 10). Measured values are consistent with low-density sedimentary deposits, massive deposits of ground-ice, or a combination of the two. This led the authors to conclude that the northern plains are made of ice-rich material to at least several tens of meters depth, which could be the remnant of a late Hesperian ocean, fed by water and sediments from outflow channels about 3 Gy ago.

3.5. Athabasca valles

The broken, rafted-plate morphology observed in the vicinity of Athabasca Valles by the High Resolution Stereo Camera has been interpreted as either due to massive fluvial discharges arising from the melting of thick ground-ice (Murray et al., 2005) or to the crystallization of a low-viscosity lava flow (Jaeger et al., 2007).

MARSIS data have been used to retrieve surface geoelectrical properties in this area to distinguish between these two hypotheses. Boisson et al. (2009) developed a method based on the time decay of the surface echo to assess the subsurface signal loss as a function of radar wave propagation time. Dielectric losses change markedly for different materials: in particular, volcanic terrains

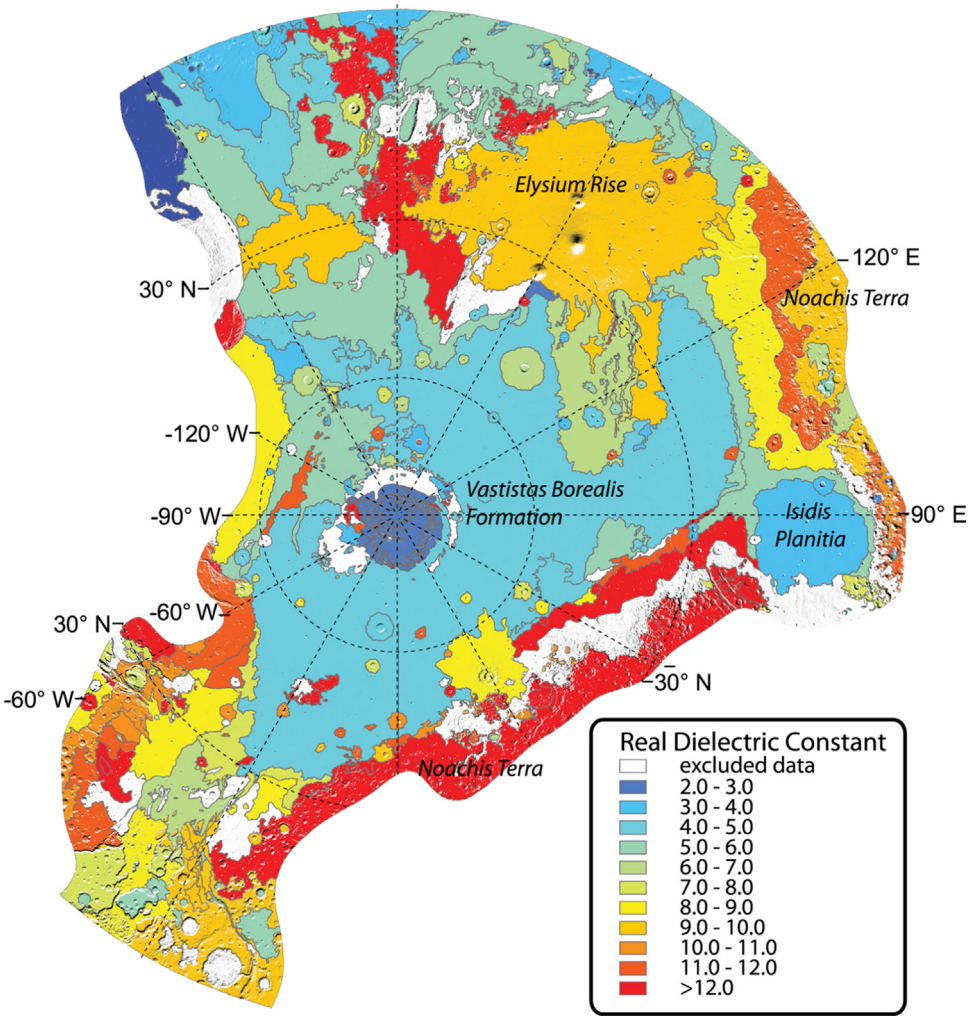

Fig. 10. Polar stereographic projection map of the Martian northern hemisphere, color-coded to indicate the MARSIS mean dielectric constant of each geological unit identified by Tanaka et al. (2005). Units where data are biased by rough surfaces are excluded and highlighted in white (from Mouginot et al., 2012). (For interpretation of the references to color in this figure caption, the reader is referred to the web version of this article.)

have much higher losses than ice-rich ones (Heggy et al., 2006; Thomson et al., 2012).

Using MARSIS data acquired along orbit 4092 between 4.5°N and 9°N latitude and centred on 149.17°E longitude, Boisson et al. (2009) calculated the average backscattered echo strength (in dB) over the ground track (Fig. 11, black thick line) as a function of radar range. The loss rate in dB/m generated by the subsurface is tied to the line slope. MARSIS observations were consistent with a mean loss over the rafted plate of 0.09 dB/m for the first 160 m of the subsurface.

This result suggests that the near-surface of Athabasca is composed of a relatively conductive material. The observed loss rate of the MARSIS signal over this region is ≈ 2 times greater than that expected for ice-rich terrains, but very similar to losses associated with basaltic rock. The dielectric characteristics of Athabasca's near-subsurface material are thus more consistent with a volcanic rather than a fluvial or mudflow origin of the rafted plate terrain, although limitations on radar sounding depth in this region cannot rule out the possibility of more deeply-buried massive ice deposits.

3.6. Study of the ionosphere using subsurface sounding data

Ionospheric distortion affecting MARSIS data was discussed in Section 2.7, where a number of possible methods to correct it was mentioned. Such methods have useful by-products, and in fact Mouginot et al. (2008) found that parameters controlling the correction through numerical maximization of the SNR were tied to the total electron content (TEC) of the ionosphere. The TEC, that is the integral of the electron density along the propagation path from the spacecraft to the Martian surface, is an important parameter in studying the ionosphere, as discussed further in Section 4.3. This quantity was thus estimated for available night-side observations and mapped over Mars by Safaeinili et al. (2007). High TEC was found in areas where field lines of crustal magnetic anomalies are perpendicular to the surface, implying that they are connected to the solar wind. Safaeinili et al. (2007) noted also that TEC values change over time in relation to solar activity.

More recently, Cartacci et al. (2013) published TEC estimates based on the contrast method. Their results on areas of high TEC confirm those by Safaeinili et al. (2007), but TEC values are often higher. A comparison of different methods for estimating TEC, including results from radio occultation and TEC estimates from AIS data, is ongoing. TEC estimates produced by Mouginot et al. (2008) have been made available through ESA's Planetary Science Archive, and have been used for scientific investigations (see e.g. Mendillo et al., 2013).

4. Main results of ionosphere sounding

In this section we shall review some of the principal results from the Active Ionospheric Sounding mode of the MARSIS radar. This will

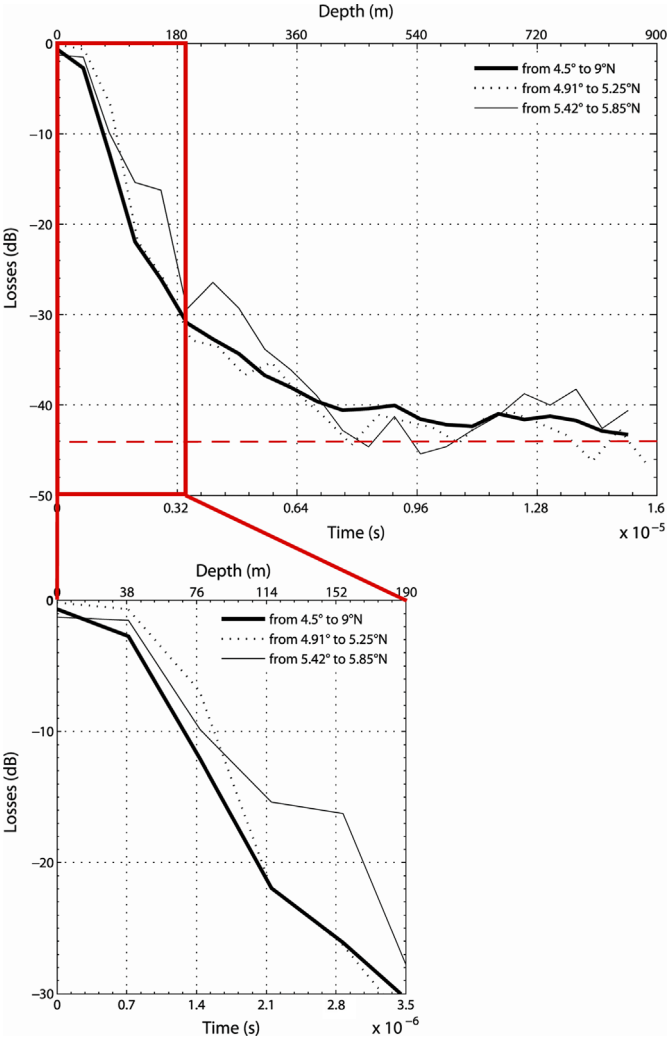

Fig. 11. Losses for radar traces between 4.5 and 9°N versus range delay time (s) and depth (m), assuming an average real relative dielectric permittivity of 7.7. The thin black line is the mean of backscattered echoes between 5.42° and 5.85°N, where there is an apparent subsurface signal. The dashed black line is the mean of backscattered echoes between 4.91° and 5.25°N. The thick black line is the mean of backscattered echoes of the study area between 4.5° and 9°N, omitting the segment from 5.42 to 5.85°N. The dashed red line represents the noise level at −42 dB. The enlargement at the bottom illustrates the loss function in the first 3.5 microseconds (red box) corresponding to an average of 160 m deep (from Boisson et al., 2009). (For interpretation of the references to color in this figure caption, the reader is referred to the web version of this article.)

include results from remote sounding, local electron density, and local magnetic field measurements. The possibilities of MARSIS AIS are summarized by Gurnett et al. (2005) and by Gurnett et al. (2008).

4.1. Local electron density from plasma frequency harmonics

The local electron densities constitute an important data set by themselves. Unlike the electron density altitude profiles, there is minimal processing involved, and they can be sorted to give easily interpreted results. An example of the use of these data is shown in Fig. 12 from Duru et al. (2008). The data compiled in this figure confirm the exponential nature of the altitude dependence above about 300 km altitude. It also shows clearly the increasing scale height of the ionosphere with increasing solar zenith angle. These data have been used extensively with ASPERA-3 ELS and IMA data (e.g. Dubinin et al., 2009). Another example of the use of local electron densities from MARSIS AIS is the mapping of a flow boundary around the Martian ionosphere, illustrated in Fig. 13 from Duru et al. (2010).

Another important result that was primarily studied with MARSIS local electron densities is the transient Martian ionopause. Duru et al. (2009) found that about 20% of the time, the boundary between the Martian magnetosheath and ionosphere sometimes takes the form of a very steep gradient in the electron density, similar to the boundary that exists between these regions at Venus. Fig. 14 shows a typical Martian ionopause as detected by MARSIS AIS electron densities.

Local electron densities from MARSIS AIS are often used in combination with data from the plasma instrument on board Mars Express, ASPERA-3. This instrument includes both an Ion Mass Analyzer (IMA) and an electron spectrometer (ELS). Using the local electron densities with ELS electron spectra gives added insight into and confirmation of results from the plasma instrument. Duru et al. (2011) found that strong depressions in the electron density on the nightside that were detected in the MARSIS local densities were sometimes accompanies by signatures of particle acceleration in both the electron and ion spectra.

Another use of this combination of data is found in the study of space weather effects, for example, as reported by Opgenoorth et al. (2013). In this study, done during an Earth–Mars period of conjunction, the effects of three space weather events, including corotation interaction regions (CIRs) and coronal mass ejections (CMEs) were studied using ASPERA-3 IMA and ELS data with the MARSIS local electron densities. These authors observed compression of the ionosphere with energization of the plasma in the region between the magnetosheath and ionosphere. A study by Morgan et al. (2014) of a single CME interaction with the Martian

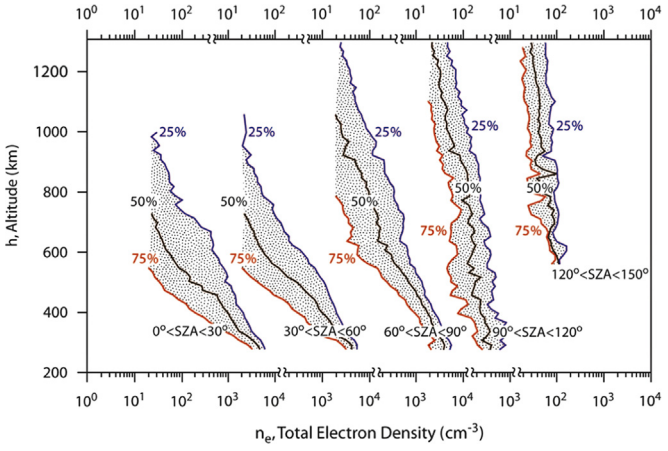

Fig. 12. Exponential variation of electron density in the upper ionosphere of Mars from the plasma frequency harmonics shown in Fig. 3 (from Duru et al., 2008).

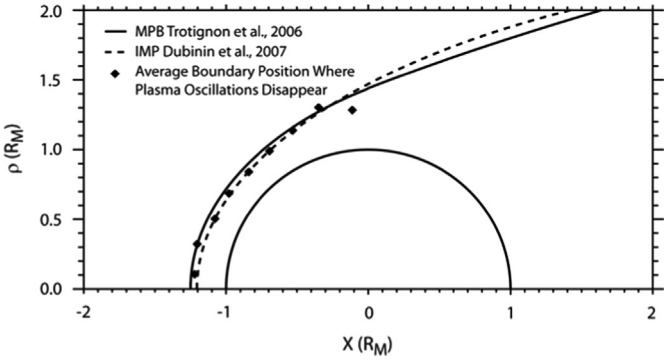

Fig. 13. Flow boundary, detected from MARSIS AIS local plasma oscillations, is seen to coincide with the magnetic pileup boundary (from Duru et al., 2010).

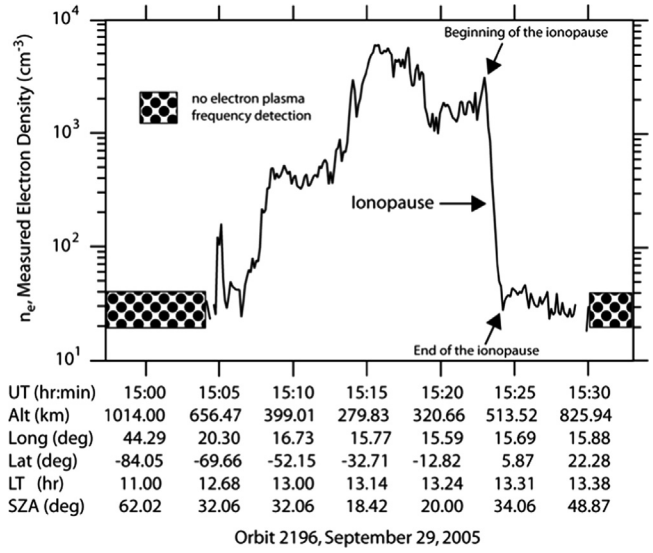

Fig. 14. Detection of the Martian ionopause using MARSIS AIS local electron densities (from Duru et al., 2009).

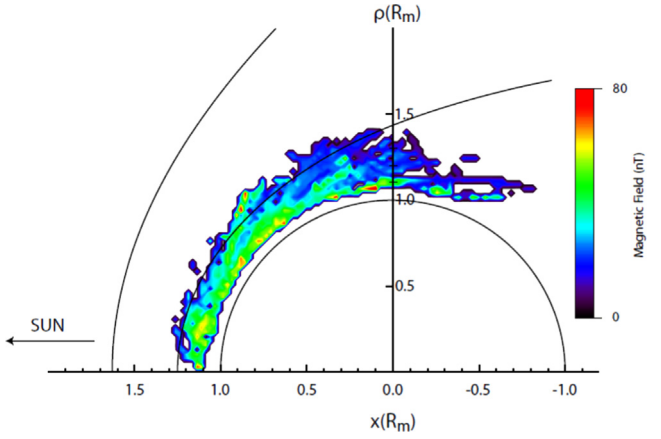

Fig. 15. Map of MARSIS AIS local magnetic field strengths with strong crustal fields excluded. The outer boundary of the detected fields is seen to coincide with the magnetic pileup boundary (from Akalin et al., 2010).

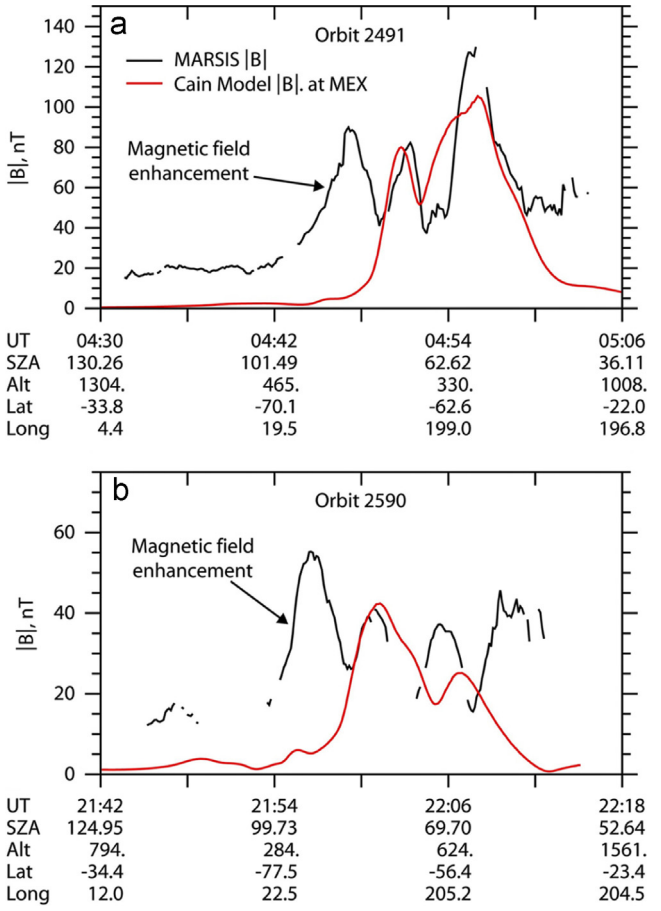

Fig. 16. MARSIS AIS magnetic field strength (black) compared to that of the Cain model (red) showing magnetic field enhancements that were not due to crustal magnetic fields (from Morgan et al., 2011). (For interpretation of the references to color in this figure caption, the reader is referred to the web version of this article.)

ionosphere, reports the compression of the ionosphere as seen by Opgenoorth et al. (2013) with apparent oscillations visible in both local electron density and local magnetic field strength. These authors also observe an extension of the ionosphere well beyond the terminator with disturbed and possibly turbulent plasma.

Finally, the local electron densities have been used to study the nightside Martian ionosphere. It was shown by Duru et al. (2011) that the scale height of the upper ionosphere on the nightside becomes much steeper, that is, there is much less variation with altitude.

4.2. *Local magnetic field strength from the electron cyclotron echoes*

The electron cyclotron harmonics shown in Fig. 3 were first explained by Gurnett et al. (2005) and Gurnett et al. (2008). Statistical results from these data were given by Akalin et al. (2010). An example is shown in Fig. 15, where the magnetic field strength, with strong crustal fields excluded, is mapped as a function of position around Mars. It can be seen that the fields detected conform with the outer limit of the magnetic pileup boundary as modelled by Dubinin et al. (2006).

A more specific topic that can be addressed through the local magnetic field strength is that of magnetic flux ropes. When we see large enhancements in the magnetic field strength that are unexplained by the presence of crustal magnetic fields as calculated by the field model developed by Cain et al. (2003) (hereinafter "the Cain model") or a similar model. The presumption is that the enhancement is caused by a magnetic flux rope. In two cases, reported by Morgan et al. (2011), a near-simultaneous detection was made with Mars Global Surveyor. By minimum variance analysis performed on the MGS magnetometer data, it was determined that the enhancements were indeed due to flux ropes. In Fig. 16, from Morgan et al. (2011), we see the two magnetic field enhancements that were unambiguously determined to be due to magnetic flux ropes. Both of these flux ropes were seen in the lee of the strongest crustal fields on Mars, close to the south pole.

4.3. *Results from remote sounding*

In previous sections we have seen ionograms, the most fundamental unit of data from MARSIS AIS. A broader outlook can be seen by selecting a range of frequencies and plotting the reflected intensities as a function of time and apparent altitude. Such a plot is shown in Fig. 17. This method of presentation has been utilized to identify "oblique echoes" seen in Fig. 17 as parabolic shaped intensifications that approach or graze the altitude of the main ionosphere. These echoes have been characterized by Duru et al. (2006) as due to off-nadir-directed radar reflections from density irregularities in the ionosphere. These irregularities are associated with intense crustal magnetic fields. A similar conclusion was reached by Nielsen et al. (2007).

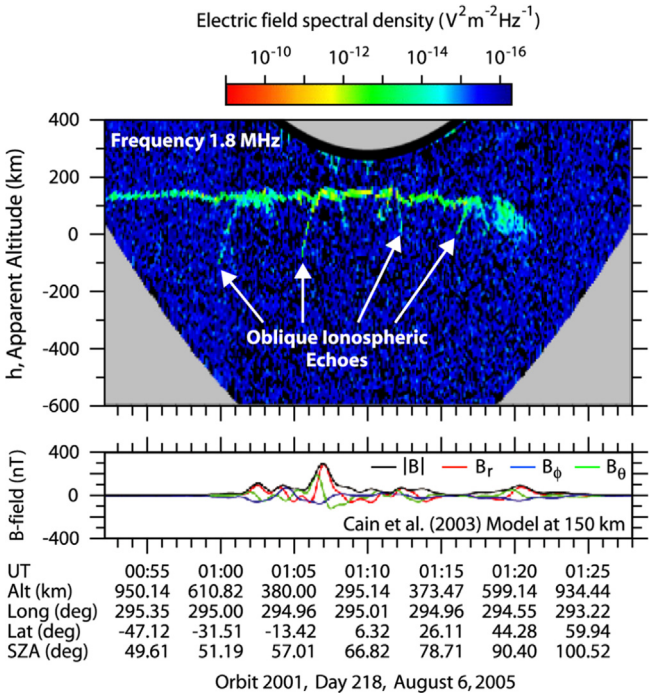

Fig. 17. "Radargram" representation of MARSIS AIS data for a single frequency as a function of time and apparent altitude. This figure clearly shows oblique echoes as parabolic shapes with apex at or near the level of the ionosphere. Below the radargram is shown the crustal magnetic field from the Cain model described by Cain et al. (2003) (from Duru et al., 2006).

The primary objective of ionospheric sounding has always been to obtain electron density profiles. Such profiles give the structure of the ionosphere, pointing to the underlying physics of its formation. The main feature of the dayside ionosphere is a main layer formed by photochemical processes initiated by EUV radiation, with peak density around 130 km altitude at the subsolar point. In addition, there is an upper ionospheric diffusion region, starting at $\approx$200 km altitude and a lower altitude layer, peaking at about 100 km, probably caused by higher energy photons and secondary electrons. The electron content of the lower layer is usually about 10% of the total. The ionospheric traces from MARSIS AIS ionograms, such as the one shown in Fig. 3, give electron density profiles for the region around the ionospheric peak near 130 km. The processed EDP for the trace shown in Fig. 3 is given in Fig. 18. The resulting profile is shown in red. The dashed line is the inferred profile between the lowest-frequency sounding reflection and the local electron density at the spacecraft from plasma frequency harmonics. When an acceptable EDP is obtained, it is often possible to fit the EDP to an ionospheric model. The usual practice has been to fit the profile to a Chapman-layer model. The result of such a fit for this case is shown in blue.

A Chapman-layer model has three parameters: The subsolar peak density, the subsolar peak density altitude, and the neutral atmosphere scale height, assumed to be constant for the entire atmosphere. In Fig. 19, we see the results of this type of fitting for about 2000 fits around the beginning of the mission. In this sampling, known periods of solar energetic particle incidence have been selected out, so that we could get a picture of the undisturbed ionosphere. During this period we found that the ionosphere appeared to have a subsolar peak density of 1.65×10^5 cm^{-3}, the subsolar peak density altitude was 130 km, and the neutral atmosphere scale height was 15 km. This period of about four and a half months was in the declining phase of solar cycle 23. It can be seen that the MARSIS AIS traces for quiet time ionosphere are fit very well by the Chapman layer model.

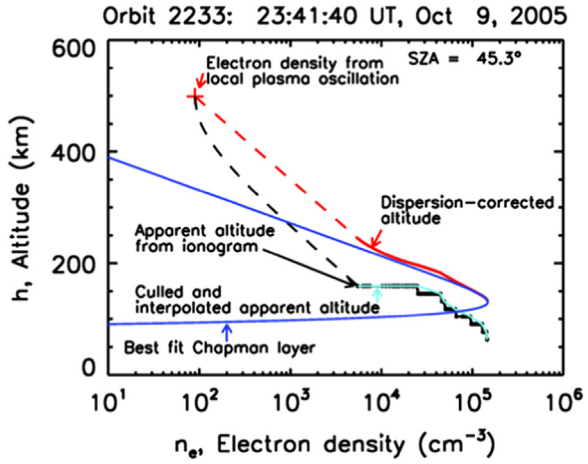

Fig. 18. EDP generated from the ionospheric trace shown in Fig. 3 (from Morgan et al., 2008).

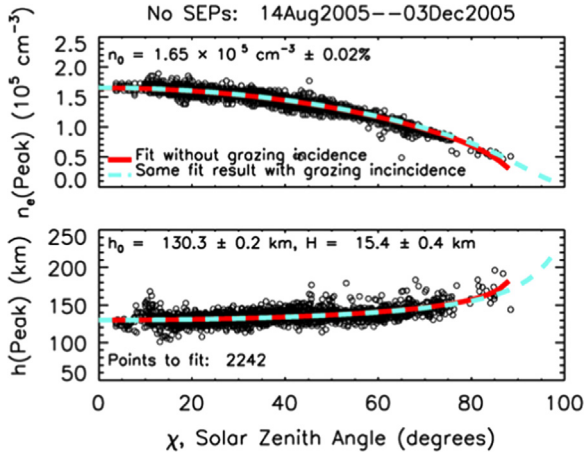

Fig. 19. Results from the fitting of ionospheric electron density profiles from MARSIS AIS to a Chapman-layer model. This sample was selected from the first 6 months of operation, with periods of strong SEP incidence culled out. It can be seen that these results are fit very will by the Chapman-layer model (from Morgan et al., 2008).

Several day-side models have been created using the MARSIS AIS traces. Němec et al. (2011b) created an empirical model using the MARSIS AIS traces. A key finding of this work was that the neutral scale height appeared to vary with altitude and also depended on the orientation of the draped magnetic field. A similar model was created by Sánchez-Cano et al. (2013). Another approach is the model of Mendillo et al. (2013), which utilizes only peak electron densities from MARSIS AIS. It is hoped that this model will be the basis of an international reference ionosphere for Mars.

The nightside ionosphere of Mars is less well organized and more difficult to analyze than the dayside. This is because the densities are much lower on the nightside; much of the time they are not visible at all. Several studies of the nightside ionosphere have been published, including Němec et al. (2010), Duru et al. (2011) (previously discussed), and Němec et al. (2011a). The last reference shows a strong relationship between the visible ionosphere in the deep nightside of Mars and regions of open crustal magnetic field lines. The prevailing picture of the patchy nightside ionosphere is that electron densities are intensified by the presence of crustal magnetic field line that are open to solar wind plasma.

Finally, we note the use of the remote sounding data to detect transient upper layers in the Martian dayside ionosphere, as reported by Kopf et al. (2008). These structures are short lived and appear to occur frequently during space weather events. The detailed dynamics are unclear, but these authors show that the distribution of these events in solar zenith angle is skewed toward the subsolar point, contra-indicating the Kelvin–Helmholtz instability as a generation mechanism.

4.4. Lightning at Mars?

It has long been speculated that the very common dust storms that occur on Mars should give rise to electrical discharges, including lightning. To test this idea, it was decided to use the MARSIS receiver as a passive detector to try to detect lightning. The study analyzed data taken over a period of five years down to a detection threshold orders of magnitude lower than typical spectral densities of lightning observed at Earth. The ionograms were sampled above frequencies of 4 MHz to avoid contamination from the ionospheric trace and plasma frequency harmonics. Pixels were also selected to avoid the surface reflection. The result of this analysis was null: no lightning was observed at Mars (Gurnett et al., 2010).

5. Current investigations

5.1. MARSIS at phobos

An unplanned development in the use of MARSIS was the successful sounding of Phobos, in spite of its small size and curved surface making it a weak radar target. MARSIS was originally designed solely for the observation of Mars, but the Martian moon could be observed during several close flybys thanks to the high eccentricity of the Mars Express orbit. For safety reasons, the radar software blocks operations when the target is closer than 240 km: to be able to operate at distances lower than that, the radar had to be re-configured to bypass protections preventing the opening of the receiver before a certain time from transmission had elapsed. Furthermore, normal on-board processing would be incapable of correctly operating, because of the relatively large uncertainties in spacecraft velocity and time of closest approach. During flybys, it was thus necessary to store raw echoes in the instrument mass memory and transmit them to the ground at a later time.

The first MARSIS opportunity to observe Phobos was on November 4th, 2005, when MARSIS came within 215 km of its surface. During this flyby, MARSIS collected data over a period of $\approx$5 min from a distance of 460 km to 215 km and then out to 430 km. A total of $\approx$16,000 raw echoes were collected and stored in instrument on-board memory. In spite of the relatively small size of Phobos and large wavelength of the radar, the observed signal to noise ratio (SNR) was $\approx$25 dB. Subsequent flybys brought MARSIS to within 100 km of the surface (Safaeinili et al., 2009).

Measurements revealed a number of secondary echoes that could be caused either by topographic relief or by subsurface interfaces. To identify surface echoes, high-resolution shape models of Phobos were used in a radar backscattering simulator based on a hybrid physical-optics and method-of-moments approach (Plettemeier et al., 2009). Running on a large scale computer cluster, the simulator was able to produce accurate, high-resolution results. Unfortunately, comparison of simulations with real data did not reveal echoes that could be positively identified as coming from the subsurface.

Simulations showed however that certain echoes were weaker or stronger than those expected for a uniform composition, presumably due to a change in dielectric properties across the surface of Phobos that affected radar reflectivity. For this reason, Hegler et al. (2011) attempted the development of a method to solve the inverse problem of determining the distribution of surface dielectric properties on Phobos, through an iterative matching between simulations and real data. The development of this method is still ongoing, although a few early results have been already presented.

Observations of Phobos remain difficult, and only a few of the flybys in which MARSIS operated produced high quality data. Optimization of instrument parameters during flybys is not without risk for the instrument, and is performed conservatively and with great care. For this reason, the lack of detection of subsurface interfaces does not rule out that they exist and can be detected in subsequent flybys. As simulations require large computational resources, not all existing data have been thoroughly analyzed. For this reason, observations of Phobos continue to be planned and executed (e.g. Cicchetti et al., 2011).

5.2. MARSIS signal inversion

The radar echo from buried structures is affected by materials crossed by the electromagnetic wave, and thus carries information on their dielectric properties. Pulses emitted by MARSIS impinge upon the Martian surface and are partly backscattered, partly diffused by surface roughness, and partly transmitted into the subsurface. The transmitted pulse in turn is attenuated by dielectric losses and scattered by any material heterogeneities. In particular, when it reaches a significant dielectric discontinuity (e.g. caused by an interface between two layers having very different electromagnetic properties), is again partly backscattered and partly transmitted.

In principle, it is possible to reconstruct a complete dielectric stratigraphy by properly analyzing the electromagnetic signal. In particular, from the analysis of backscattered signal features it is possible to retrieve the dielectric permittivity of layers and, under favorable conditions, their structure and composition. Reconstruction of the dielectric stratigraphy from the received echo is a nonlinear inverse problem, whose solution for MARSIS has been attempted in a limited number of cases. Given the complexity of problems of this type and the almost complete lack of information on the Martian subsurface, treatment inevitably required some simplifications or assumptions.

In the general theoretical framework described in Picardi (2004), Picardi et al. (2008) first attempted the retrieval of the permittivity at the bottom of the SPLD in an area of very low topographic roughness. Dielectric properties of the basal layer were estimated starting from the ratio between the power of the signal reflected by the atmosphere/surface interface and that of the signal reflected by the interface between SPLD and the underlying bedrock. The applied inversion technique was based on the modelling of a plane electromagnetic wave propagating normally through three homogeneous non-magnetic layers: an upper semi-infinite layer representing the atmosphere; a second layer representing the SPLD; and a third semi-infinite layer representing the material beneath the SPLD. By estimating individual factors affecting subsurface echo power, the dielectric contrast between SPLD and bedrock could be derived. Results remained inconclusive, however, as the extent of signal attenuation within the SPLD could not be constrained with confidence.

The ratio between subsurface and surface reflections over a portion of the SPLD was used also by Zhang et al. (2008) to develop a different approach to inversion, based on Bayesian inference. Through the parametric forward modelling of propagation through the SPLD and the derivation of the statistical distribution of subsurface-to-surface echo power ratio, they applied a genetic algorithm to estimate the most likely set of physical parameters

producing the observed echoes. Also in this case, modelling assumed a plane electromagnetic wave propagating normally through three homogeneous non-magnetic layers. In their analysis, Zhang et al. (2008) found a large sensitivity of the solution to small changes in initial conditions, making this an ill-posed problem. It was found that the most probable value of the relative dielectric constant of the SPLD lay between 3.0 and 5.0, and that the relative dielectric constant of the basal layer was between 7.5 and 8.5, a value typical of basalts. These results support the interpretation that the SPLD are made of water ice/dust mixtures with dust content varying from 0 to more than 75%.

Lauro et al. (2010) developed a simpler methodology using the same modelling of propagation and the same measured quantities of previous works, but applying it to the NPLD in an area within Gemina Lingula. They reduced uncertainties in the estimation of attenuation within the NPLD, which affected conclusions by Picardi et al. (2008), through the modelling of their dielectric permittivity based on information on their composition, derived from other datasets. They obtained estimates for the dielectric permittivity of the bedrock comprised between 4 and 9, in the range typical for basalts thought to constitute the Martian crust. This method was found to be more stable compared to previous works, but its applicability is limited by the need to obtain information on the composition of subsurface layers through other sources.

Overall, methods developed so far to extract quantitative information on the nature of subsurface layers are affected by large uncertainties, and can be applied only in a limited number of favorable conditions. It can thus be concluded that much work has still to be done, but potential results outweigh difficulties: as the dielectric permittivity of liquid water is much greater than that of rock or ices, a reliable detection of a subsurface layer with a dielectric constant well above that typical of other geologic materials could be plausibly explained as due to the presence of water, a finding that would change the entire perspective of Martian exploration.

6. Conclusions

MARSIS was the first radar sounder since the ALSE experiment on board Apollo 17, and the first instrument of its kind to be ever flown to Mars. In spite of the many risks and difficulties faced in the initial phase of the Mars Express mission, it has been operating successfully since 2005, and shows no sign of performance degradation.

Analysis of radar data was made difficult by several artefacts affecting the signal, from ionosphere distortion to lateral surface echoes to apparent deformation of subsurface interfaces due to variations of the refraction index in different materials. Because of the lack of a consolidated background of experience on similar experiments, most solutions to these problems had to be devised from scratch and tested only once MARSIS was already operating.

In spite of this, MARSIS has produced unique data that gave proof of hypotheses that could not have been tested otherwise, such as the predominantly icy composition of the Polar Layered Deposits and the presence of water ice down to depths of several tens of meters in Vastitas Borealis, revealing also phenomena such as the complex interaction between the Martian ionosphere and its residual magnetic field, and the high ice content of the Dorsa Argentea formation. By successfully operating at Phobos, MARSIS performed above and beyond its requirements and became the first instrument of its kind to observe an asteroid-like body. As interest for this class of bodies increases, driven by economic and security factors as well as by scientific interest, the dataset produced by MARSIS will become a key factor in designing future missions.

The main goal pursued by MARSIS, the detection of liquid water beneath the surface, remains elusive. While the radar penetrated to a depth of more than 3.7 km in ice-rich polar terrains, in rocky terrains detections have been reported at depths of slightly more than 2.5 km under favorable conditions. Is this sufficient to determine if the Martian water table exists?

Liquid water can persist in the subsurface for extended periods of time only below the cryosphere, which is the region of the crust where temperature remains continuously below the freezing point. Estimates of its present thickness range from a few to several km, depending on ill-known parameters such as thermal properties of the crust and present-day global heat flow (Clifford et al., 2010). Farrell et al. (2009) investigated the capability of MARSIS to detect a water table beneath the cryosphere, but the range of variability for the electromagnetic parameters of the crust is so large that the lack of direct detection does not rule out the possibility of the water table's existence. Recent estimates of cryosphere thickness resulted in greater depths for the possible presence of water (Clifford et al., 2010), decreasing the likelihood of detection through MARSIS. In spite of this, substantial local variations of physical parameters controlling the cryosphere may occur (Clifford et al., 2010), leading to favorable conditions for direct observation of subsurface water. As coverage of Mars is still incomplete, also due to factors affecting the quality of observations such as solar activity and illumination conditions, the search continues.

Even if water is within the reach of MARSIS, however, detection does not mean identification: only a sufficiently precise determination of the dielectric properties of the subsurface layer causing the reflection can confirm the presence of water in the Martian subsurface. For this reason, the development of accurate methods for the inversion of the MARSIS signal remains the main priority for theoretical development supporting data interpretation.

Acknowledgments

This work was supported by the Italian Space Agency (ASI) through Contract no. I/032/12/0. This research has made use of NASA's Astrophysics Data System.

References

Akalin, F., Morgan, D.D., Gurnett, D.A., Kirchner, D.L., Brain, D.A., Modolo, R., Acuña, M.H., Espley, J.R., 2010. Dayside induced magnetic field in the ionosphere of Mars. Icarus 206, 104–111. http://dx.doi.org/10.1016/j.icarus.2009.03.021.

Andrews, D.J., Opgenoorth, H.J., Edberg, N.J.T., André, M., Fränz, M., Dubinin, E., Duru, F., Morgan, D.D., Witasse, O., 2013. Determination of local plasma densities with the MARSIS radar: asymmetries in the high-altitude Martian ionosphere. J. Geophys. Res. 118. http://dx.doi.org/10.1002/jgra.50593.

Benson, R.F., 2010. Four decades of space-borne radio sounding. Radio Sci. Bull., 24–44.

Benson, R.F., Bilitza, D., 2009. New satellite mission with old data: rescuing a unique data set. Radio Sci. 44, http://dx.doi.org/10.1029/2008RS004036.

Boisson, J., Heggy, E., Clifford, S.M., Frigeri, A., Plaut, J.J., Farrell, W.M., Putzig, N.E., Picardi, G., Orosei, R., Lognonné, P., Gurnett, D.A., 2009. Sounding the subsurface of Athabasca Valles using MARSIS radar data: exploring the volcanic and fluvial hypotheses for the origin of the rafted plate terrain. J. Geophys. Res. (Planets) 114, 8003. http://dx.doi.org/10.1029/2008JE003299.

Budden, K.G., 1961. Radio Waves in the Ionosphere. Cambridge University Press, London, UK.

Byrne, S., 2009. The polar deposits of mars. Annu. Rev. Earth Planet. Sci. 37, 535–560. http://dx.doi.org/10.1146/annurev.earth.031208.100101.

Byrne, S., Murray, B.C., 2002. North polar stratigraphy and the paleo-erg of Mars. J. Geophys. Res. (Planets) 107, 5044. http://dx.doi.org/10.1029/2001JE001615.

Cain, J.C., Ferguson, B.B., Mozzoni, D., 2003. An n=90 internal potential function of the Martian crustal magnetic field. J. Geophys. Res. (Planets) 108, 5008 http://dx.doi.org/10.1029/2000JE001487.

Carrier III, W.D., Olhoeft, G.R., Mendell, W., 1991. Physical properties of the lunar surface. In: Heiken, G.H., Vaniman, D.T., French, B.M. (Eds.), Lunar Sourcebook. Cambridge University Press, Cambridge, New York, pp. 475–594.

Cartacci, M., Amata, E., Cicchetti, A., Noschese, R., Giuppi, S., Langlais, B., Frigeri, A., Orosei, R., Picardi, G., 2013. Mars ionosphere total electron content analysis from MARSIS subsurface data. Icarus 223, 423–437. http://dx.doi.org/10.1016/j.icarus.2012.12.011.

Cartacci, M., Frigeri, A., Orosei, R., Pettinelli, E., 2008. Surface and Subsurface Radar Backscattering Coefficient over the Martian South Polar Layered Deposits From MARSIS Data. AGU Fall Meeting Abstracts, p. B1466.

Chicarro, A., Martin, P., Trautner, R., 2004. The Mars Express mission: an overview. In: Wilson, A., Chicarro, A. (Eds.), Mars Express: The Scientific Payload vol. 1240. ESA Special Publication, Noordwijk, The Netherlands, pp. 3–13.

Cicchetti, A., Cartacci, M., Gim, Y., Giuppi, S., Heggy, E., Hegler, S., Ivanov, A.B., Nenna, C., Noschese, R., Orosei, R., Plaut, J.J., Plettemeier, D., Seu, R., 2011. MARSIS: latest phobos flyby. Data processing results and advanced radar configuration design. In: EPSC-DPS Joint Meeting 2011, p. 497.

Clifford, S.M., Lasue, J., Heggy, E., Boisson, J., McGovern, P., Max, M.D., 2010. Depth of the Martian cryosphere: revised estimates and implications for the existence and detection of subpermafrost groundwater. J. Geophys. Res. Planets 115, 7001. http://dx.doi.org/10.1029/2009JE003462.

Dubinin, E., Fraenz, M., Woch, J., Duru, F., Gurnett, D., Modolo, R., Barabash, S., Lundin, R., 2009. Ionospheric storms on Mars: impact of the corotating interaction region. Geophys. Res. Lett. 36, 1105. http://dx.doi.org/10.1029/2008GL036559.

Dubinin, E., Fränz, M., Woch, J., Roussos, E., Barabash, S., Lundin, R., Winningham, J.D., Frahm, R.A., Acuna, M., 2006. Plasma morphology at Mars. Aspera-3 Observations. Space Sci. Rev. 126, 209–238. http://dx.doi.org/10.1007/s11214-006-9039-4.

Duru, F., Gurnett, D.A., Averkamp, T.F., Kirchner, D.L., Huff, R.L., Persoon, A.M., Plaut, J.J., Picardi, G., 2006. Magnetically controlled structures in the ionosphere of Mars. J. Geophys. Res. (Space Phys.) 111, 12204. http://dx.doi.org/10.1029/2006JA011975.

Duru, F., Gurnett, D.A., Frahm, R.A., Winningham, J.D., Morgan, D.D., Howes, G.G., 2009. Steep, transient density gradients in the Martian ionosphere similar to the ionopause at Venus. J. Geophys. Res. (Space Phys.) 114, 12310. http://dx.doi.org/10.1029/2009JA014711.

Duru, F., Gurnett, D.A., Morgan, D.D., Modolo, R., Nagy, A.F., Najib, D., 2008. Electron densities in the upper ionosphere of Mars from the excitation of electron plasma oscillations. J. Geophys. Res. (Space Phys.) 113, 7302. http://dx.doi.org/10.1029/2008JA013073.

Duru, F., Gurnett, D.A., Morgan, D.D., Winningham, J.D., Frahm, R.A., Nagy, A.F., 2011. Nightside ionosphere of Mars studied with local electron densities: a general overview and electron density depressions. J. Geophys. Res. (Space Phys.) 116, 10316. http://dx.doi.org/10.1029/2011JA016835.

Duru, F., Gurnett, D.A., Winningham, J.D., Frahm, R., Modolo, R., 2010. A plasma flow velocity boundary at Mars from the disappearance of electron plasma oscillations. Icarus 206, 74–82. http://dx.doi.org/10.1016/j.icarus.2009.04.012.

Farrell, W.M., Clifford, S.M., Milkovich, S.M., Plaut, J.J., Leuschen, C.J., Picardi, G., Gurnett, D.A., Watters, T.R., Safaeinili, A., Ivanov, A.B., Phillips, R.J., Stofan, E.R., Heggy, E., Cummer, S.A., Espley, J.R., 2008. MARSIS subsurface radar investigations of the South Polar reentrant Chasma Australe. J. Geophys. Res. (Planets) 113, 4002. http://dx.doi.org/10.1029/2007JE002974.

Farrell, W.M., Plaut, J.J., Cummer, S.A., Gurnett, D.A., Picardi, G., Watters, T.R., Safaeinili, A., 2009. Is the Martian water table hidden from radar view? Geophys. Res. Lett. 36, 15206. http://dx.doi.org/10.1029/2009GL038945.

Franklin, C.A., Maclean, M.A., 1969. The design of swept-frequency topside sounders. Proc. IEEE 57, 897–929.

Frigeri, A., Orosei, R., Cartacci, M., Cicchetti, A., Mitri, G., Giuppi, S., Noschese, R., Picardi, G., Plaut, J.J., 2012. Three dimensional structure and possible lateral inhomogeneities of the Mars North Polar Basal Unit. In: Lunar and Planetary Institute Science Conference Abstracts, Lunar and Planetary Institute Science Conference Abstracts, vol. 43, p. 2922.

Gurnett, D.A., Huff, R.L., Morgan, D.D., Persoon, A.M., Averkamp, T.F., Kirchner, D.L., Duru, F., Akalin, F., Kopf, A.J., Nielsen, E., Safaeinili, A., Plaut, J.J., Picardi, G., 2008. An overview of radar soundings of the martian ionosphere from the Mars Express spacecraft. Adv. Space Res. 41, 1335–1346. http://dx.doi.org/10.1016/j.asr.2007.01.062.

Gurnett, D.A., Kirchner, D.L., Huff, R.L., Morgan, D.D., Persoon, A.M., Averkamp, T.F., Duru, F., Nielsen, E., Safaeinili, A., Plaut, J.J., Picardi, G., 2005. Radar soundings of the ionosphere of Mars. Science 310, 1929–1933. http://dx.doi.org/10.1126/science.1121868.

Gurnett, D.A., Morgan, D.D., Granroth, L.J., Cantor, B.A., Farrell, W.M., Espley, J.R., 2010. Non-detection of impulsive radio signals from lightning in Martian dust storms using the radar receiver on the Mars Express spacecraft. Geophys. Res. Lett. 37, 17802. http://dx.doi.org/10.1029/2010GL044368.

Heggy, E., Clifford, S.M., Grimm, R.E., Dinwiddie, C.L., Wyrick, D.Y., Hill, B.E., 2006. Ground-penetrating radar sounding in mafic lava flows: assessing attenuation and scattering losses in Mars-analog volcanic terrains. J. Geophys. Res. (Planets) 111, 6. http://dx.doi.org/10.1029/2005JE002589.

Hegler, S., Statz, C., Plettemeier, D., Cicchetti, A., Ivanov, A.B., Orosei, R., 2011. Surface epsilon_r reconstruction of Phobos. In: EPSC-DPS Joint Meeting 2011, p. 1349.

Hynek, B.M., Phillips, R.J., Arvidson, R.E., 2003. Explosive volcanism in the Tharsis region: global evidence in the Martian geologic record. J. Geophys. Res. (Planets) 108, 5111. http://dx.doi.org/10.1029/2003JE002062.

Ilyushin, Y.A., Kunitsyn, V.E., 2004. Methods for correcting ionosphere distortions of orbital ground-penetrating radar signals. J. Commun. Technol. Electron. 49, 154–165.

Jackson, J.E., 1969. The reduction of topside Ionograms to electron-density profiles. Proc. IEEE 57, 960–975.

Jaeger, W.L., Keszthelyi, L.P., McEwen, A.S., Dundas, C.M., Russell, P.S., 2007. Athabasca Valles, Mars: a lava-draped channel system. Science 317, 1709. http://dx.doi.org/10.1126/science.1143315.

Jordan, R., Picardi, G., Plaut, J., Wheeler, K., Kirchner, D., Safaeinili, A., Johnson, W., Seu, R., Calabrese, D., Zampolini, E., Cicchetti, A., Huff, R., Gurnett, D., Ivanov, A., Kofman, W., Orosei, R., Thompson, T., Edenhofer, P., Bombaci, O., 2009. The Mars express MARSIS sounder instrument. Planet. Space Sci. 57, 1975–1986. http://dx.doi.org/10.1016/j.pss.2009.09.016.

Kerber, L., Head, J.W., 2010. The age of the Medusae Fossae Formation: evidence of Hesperian emplacement from crater morphology, stratigraphy, and ancient lava contacts. Icarus 206, 669–684. http://dx.doi.org/10.1016/j.icarus.2009.10.001.

Kerber, L., Head, J.W., Madeleine, J.-B., Forget, F., Wilson, L., 2011. The dispersal of pyroclasts from Apollinaris Patera, Mars: implications for the origin of the Medusae Fossae Formation. Icarus 216, 212–220. http://dx.doi.org/10.1016/j.icarus.2011.07.035.

Kopf, A.J., Gurnett, D.A., Morgan, D.D., Kirchner, D.L., 2008. Transient layers in the topside ionosphere of Mars. Geophys. Res. Lett. 35, 17102. http://dx.doi.org/10.1029/2008GL034948.

Kreslavsky, M.A., Head, J.W., 2002. Fate of outflow channel effluents in the northern lowlands of Mars: the Vastitas Borealis Formation as a sublimation residue from frozen ponded bodies of water. J. Geophys. Res. (Planets) 107, 5121. http://dx.doi.org/10.1029/2001JE001831.

Lanagan, P.D., McEwen, A.S., Keszthelyi, L.P., Thordarson, T., 2001. Rootless cones on Mars indicating the presence of shallow equatorial ground ice in recent times. Geophys. Res. Lett. 28, 2365–2367. http://dx.doi.org/10.1029/2001GL012932.

Langevin, Y., Poulet, F., Bibring, J.-P., Schmitt, B., Douté, S., Gondet, B., 2005. Summer evolution of the North Polar Cap of Mars as observed by OMEGA/Mars Express. Science 307, 1581–1584. http://dx.doi.org/10.1126/science.1109438.

Lauro, S.E., Mattei, E., Pettinelli, E., Soldovieri, F., Orosei, R., Cartacci, M., Cicchetti, A., Noschese, R., Giuppi, S., 2010. Permittivity estimation of layers beneath the northern polar layered deposits, Mars. Geophys. Res. Lett. 37, 14201. http://dx.doi.org/10.1029/2010GL043015.

Mandt, K.E., deSilva, S.L., Zimbelman, J.R., Crown, D.A., 2008. Origin of the medusae fossae formation, Mars: insights from a synoptic approach. J. Geophys. Res. (Planets) 113, 12011. http://dx.doi.org/10.1029/2008JE003076.

Mendillo, M., Narvaez, C., Withers, P., Matta, M., Kofman, W., Mouginot, J., 2013. Variability in ionospheric total electron content at Mars. Planet. Space Sci. 86, 117–129. http://dx.doi.org/10.1016/j.pss.2013.08.010.

Milkovich, S.M., Plaut, J.J., Safaeinili, A., Picardi, G., Seu, R., Phillips, R.J., 2009. Stratigraphy of Promethei Lingula, south polar layered deposits, Mars, in radar and imaging data sets. J. Geophys. Res. (Planets) 114, 3002. http://dx.doi.org/10.1029/2008JE003162.

Morgan, D.D., Diéval, C., Gurnett, D.A., Duru, F., Dubinin, E.M., Fränz, M., Andrews, D. J., Opgenoorth, H.J., Ulusen, D., Mitrofanov, I., Plaut, J.J., 2014. Effects of a strong ICME on the martian ionosphere as detected by Mars Express and Mars Odyssey. J. Geophys. Res. (Space Phys.) 119 (7), 5891–5908. http://dx.doi.org/10.1002/2013JA019522.

Morgan, D.D., Gurnett, D.A., Akalin, F., Brain, D.A., Leisner, J.S., Duru, F., Frahm, R.A., Winningham, J.D., 2011. Dual-spacecraft observation of large-scale magnetic flux ropes in the Martian ionosphere. J. Geophys. Res. (Space Phys.) 116, 2319. http://dx.doi.org/10.1029/2010JA016134.

Morgan, D.D., Gurnett, D.A., Kirchner, D.L., DavidWinningham, J., Frahm, R.A., Brain, D.A., Mitchell, D.L., Luhmann, J.G., Nielsen, E., Espley, J.R., Acuña, M.H., Plaut, J.J., 2010. Radar absorption due to a corotating interaction region encounter with Mars detected by MARSIS. Icarus 206, 95–103. http://dx.doi.org/10.1016/j.icarus.2009.03.008.

Morgan, D.D., Gurnett, D.A., Kirchner, D.L., Fox, J.L., Nielsen, E., Plaut, J.J., 2008. Variation of the Martian ionospheric electron density from Mars Express radar soundings. J. Geophys. Res. (Space Phys.) 113, 9303. http://dx.doi.org/10.1029/2008JA013313.

Morgan, D.D., Gurnett, D.A., Kirchner, D.L., Fox, J.L., Nielsen, E., Plaut, J.J., 2013a. Correction to Variation of the Martian ionospheric electron density from Mars Express radar soundings. J. Geophys. Res. (Space Phys.) 118, http://dx.doi.org/10.1002/jgra.50369 4710–4710.

Morgan, D.D., Gurnett, D.A., Kirchner, D.L., Huff, R.L., Brain, D.A., Boynton, W.V., Acuña, M.H., Plaut, J.J., Picardi, G., 2006. Solar control of radar wave absorption by the Martian ionosphere. Geophys. Res. Lett. 33, 13202. http://dx.doi.org/10.1029/2006GL026637.

Morgan, D.D., Witasse, O., Nielsen, E., Gurnett, D.A., Duru, F., Kirchner, D.L., 2013b. The processing of electron density profiles from the Mars Express MARSIS topside sounder. Radio Sci. 48, 197–207. http://dx.doi.org/10.1002/rds.20023.

Mouginot, J., Kofman, W., Safaeinili, A., Grima, C., Herique, A., Plaut, J.J., 2009. MARSIS surface reflectivity of the south residual cap of Mars. Icarus 201, 454–459. http://dx.doi.org/10.1016/j.icarus.2009.01.009.

Mouginot, J., Kofman, W., Safaeinili, A., Herique, A., 2008. Correction of the ionospheric distortion on the MARSIS surface sounding echoes. Planet. Space Sci. 56, 917–926. http://dx.doi.org/10.1016/j.pss.2008.01.010.

Mouginot, J., Pommerol, A., Beck, P., Kofman, W., Clifford, S.M., 2012. Dielectric map of the Martian northern hemisphere and the nature of plain filling materials. Geophys. Res. Lett. 39, 2202. http://dx.doi.org/10.1029/2011GL050286.

Mouginot, J., Pommerol, A., Kofman, W., Beck, P., Schmitt, B., Herique, A., Grima, C., Safaeinili, A., Plaut, J.J., 2010. The 3–5 MHz global reflectivity map of Mars by MARSIS/Mars Express: implications for the current inventory of subsurface H_2O. Icarus 210, 612–625. http://dx.doi.org/10.1016/j.icarus.2010.07.003.

Murray, J.B., Muller, J.-P., Neukum, G., Werner, S.C., van Gasselt, S., Hauber, E., Markiewicz, W.J., Head, J.W., Foing, B.H., Page, D., Mitchell, K.L., Portyankina, G., HRSC Co-Investigator Team, 2005. Evidence from the mars express high resolution Stereo Camera for a frozen sea close to Mars' equator. Nature 434, 352–356. http://dx.doi.org/10.1038/nature03379.

Nielsen, E., Fraenz, M., Zou, H., Wang, J.-S., Gurnett, D.A., Kirchner, D.L., Morgan, D.D., Huff, R., Safaeinili, A., Plaut, J.J., Picardi, G., Winningham, J.D., Frahm, R.A., Lundin, R., 2007. Local plasma processes and enhanced electron densities in the lower ionosphere in magnetic cusp regions on Mars. Planet. Space Sci. 55, 2164–2172. http://dx.doi.org/10.1016/j.pss.2007.07.003.

Nouvel, J.-F., Herique, A., Kofman, W., Safaeinili, A., 2004. Radar signal simulation: surface modeling with the Facet Method. Radio Sci. 39, 1013. http://dx.doi.org/10.1029/2003RS002903.

Němec, F., Morgan, D.D., Gurnett, D.A., Brain, D.A., 2011a. Areas of enhanced ionization in the deep nightside ionosphere of Mars. J. Geophys. Res. (Planets) 116, 6006. http://dx.doi.org/10.1029/2011JE003804.

Němec, F., Morgan, D.D., Gurnett, D.A., Duru, F., 2010. Nightside ionosphere of Mars: radar soundings by the Mars Express spacecraft. J. Geophys. Res. (Planets) 115, 12009. http://dx.doi.org/10.1029/2010JE003663.

Němec, F., Morgan, D.D., Gurnett, D.A., Duru, F., Truhlík, V., 2011b. Dayside ionosphere of Mars: empirical model based on data from the MARSIS instrument. J. Geophys. Res. (Planets) 116, 7003. http://dx.doi.org/10.1029/2010JE003789.

Opgenoorth, H.J., Andrews, D.J., Fränz, M., Lester, M., Edberg, N.J.T., Morgan, D.D., Duru, F., Witasse, O., Williams, A.O., 2013. Mars ionospheric response to solar wind variability. J. Geophys. Res. 118. http://dx.doi.org/10.1002/jgra.50537.

Picardi, G., 2004. Radar for measuring interplanetary bodies. In: Daniels, D.J. (Ed.), Ground Penetrating Radar, 2nd ed. Institution of Engineering and Technology, London, UK, pp. 663–686.

Picardi, G., Biccari, D., Cartacci, M., Cicchetti, A., Giuppi, S., Marini, A., Masdea, A., Noschese, R., Piccari, F., Seu, R., Plaut, J.J., Johnson, W., Jordan, R.L., Safaeinili, A., Federico, C., Frigeri, A., Melacci, P.T., Orosei, R., Bombaci, O., Calabrese, D., Zampolini, E., Edenhofer, P., Plettemeier, D., Marinangeli, L., Pettinelli, E., Hagfors, T., Flamini, E., Vannaroni, G., Nielsen, E., Williams, I., Gurnett, D., Kirchner, D., Huff, R., 2008. Marsis data inversion approach: preliminary results. In: 2008 IEEE Radar Conference. IEEE Conference Publications, pp. 1–4.

Picardi, G., Biccari, D., Seu, R., Marinangeli, L., Johnson, W.T.K., Jordan, R.L., Plaut, J., Safaenili, A., Gurnett, D.A., Ori, G.G., Orosei, R., Calabrese, D., Zampolini, E., 2004a. Performance and surface scattering models for the Mars Advanced Radar for Subsurface and Ionosphere Sounding (MARSIS). Planet. Space Sci. 52, 149–156. http://dx.doi.org/10.1016/j.pss.2003.08.020.

Picardi, G., Biccari, D., Seu, R., Plaut, J., Johnson, W.T.K., Jordan, R.L., Safaeinili, A., Gurnett, D.A., Huff, R., Orosei, R., Bombaci, O., Calabrese, D., Zampolini, E., 2004b. MARSIS: Mars advanced radar for subsurface and ionosphere sounding. In: Wilson, A., Chicarro, A. (Eds.), Mars Express: The Scientific Payload vol. 1240. ESA Special Publication, Noordwijk, The Netherlands, pp. 51–69.

Picardi, G., Plaut, J.J., Biccari, D., Bombaci, O., Calabrese, D., Cartacci, M., Cicchetti, A., Clifford, S.M., Edenhofer, P., Farrell, W.M., Federico, C., Frigeri, A., Gurnett, D.A., Hagfors, T., Heggy, E., Herique, A., Huff, R.L., Ivanov, A.B., Johnson, W.T.K., Jordan, R.L., Kirchner, D.L., Kofman, W., Leuschen, C.J., Nielsen, E., Orosei, R., Pettinelli, E., Phillips, R.J., Plettemeier, D., Safaeinili, A., Seu, R., Stofan, E.R., Vannaroni, G., Watters, T.R., Zampolini, E., 2005. Radar soundings of the subsurface of Mars. Science 310, 1925–1928. http://dx.doi.org/10.1126/science.1122165.

Plaut, J.J., Frigeri, A., Orosei, R., 2012. Compositional constraints on the Martian North Polar Basal Unit from MARSIS radar sounding data. In: Lunar and Planetary Institute Science Conference Abstracts, Lunar and Planetary Institute Science Conference Abstracts, vol. 43, p. 2458.

Plaut, J.J., Ivanov, A., Safaeinili, A., Milkovich, S.M., Picardi, G., Seu, R., Phillips, R., 2007a. Radar sounding of subsurface layers in the South Polar Plains of Mars: correlation with the Dorsa Argentea Formation. In: Lunar and Planetary Institute Science Conference Abstracts, Lunar and Planetary Institute Science Conference Abstracts, vol. 38, p. 2144.

Plaut, J.J., Picardi, G., Safaeinili, A., Ivanov, A.B., Milkovich, S.M., Cicchetti, A., Kofman, W., Mouginot, J., Farrell, W.M., Phillips, R.J., Clifford, S.M., Frigeri, A., Orosei, R., Federico, C., Williams, I.P., Gurnett, D.A., Nielsen, E., Hagfors, T., Heggy, E., Stofan, E.R., Plettemeier, D., Watters, T.R., Leuschen, C.J., Edenhofer, P., 2007b. Subsurface radar sounding of the south polar layered deposits of Mars. Science 316, 92. http://dx.doi.org/10.1126/science.1139672.

Plettemeier, D., Hahnel, R., Hegler, S., Safaeinili, A., Orosei, R., Cicchetti, A., Plaut, J., Picardi, G., 2009. Simulation of radar-backscattering from phobos—a contribution to the experiment MARSIS aboard MarsExpress. In: Arabelos, D.N., Tscherning, C. C. (Eds.), EGU General Assembly Conference Abstracts. EGU General Assembly Conference Abstracts, vol. 11. p. 3763.

Porcello, L.J., Jordan, R.L., Zelenka, J.S., Adams, G.F., Phillips, R.J., Brown Jr., W.E., Ward, S.H., Jackson, P.L., 1974. The Apollo lunar sounder radar system. IEEE Proc. 62, 769–783.

Rishbeth, H., Garriott, O.K., 1969. Introduction to Ionospheric Physics.

Safaeinili, A., Cicchetti, A., Nenna, C., Calabrese, D., Plettemeier, D., Orosei, R., Duxbury, T., Plaut, J.J., Picardi, G., Flamini, E., 2009. Radar sounder observations of phobos. In: European Planetary Science Congress, p. 717.

Safaeinili, A., Kofman, W., Mouginot, J., Gim, Y., Herique, A., Ivanov, A.B., Plaut, J.J., Picardi, G., 2007. Estimation of the total electron content of the Martian ionosphere using radar sounder surface echoes. Geophys. Res. Lett. 34, 23204. http://dx.doi.org/10.1029/2007GL032154.

Safaeinili, A., Kofman, W., Nouvel, J.-F., Herique, A., Jordan, R.L., 2003. Impact of Mars ionosphere on orbital radar sounder operation and data processing. Planet. Space Sci. 51, 505–515. http://dx.doi.org/10.1016/S0032-0633(03)00048-5.

Sánchez-Cano, B., Radicella, S.M., Herraiz, M., Witasse, O., Rodríguez-Caderot, G., 2013. NeMars: an empirical model of the martian dayside ionosphere based on Mars Express MARSIS data. Icarus 225, 236–247. http://dx.doi.org/10.1016/j.icarus.2013.03.021.

Scott, D.H., Tanaka, K.L., 1986. Geologic Map of the Western Equatorial Region of Mars. Miscellaneous Investigations Series Map I-1802-A U.S. Geological Survey.

Selvans, M.M., Plaut, J.J., Aharonson, O., Safaeinili, A., 2010. Internal structure of Planum Boreum, from Mars advanced radar for subsurface and ionospheric sounding data. J. Geophys. Res. (Planets) 115, 9003. http://dx.doi.org/10.1029/2009JE003537.

Seu, R., Phillips, R.J., Biccari, D., Orosei, R., Masdea, A., Picardi, G., Safaeinili, A., Campbell, B.A., Plaut, J.J., Marinangeli, L., Smrekar, S.E., Nunes, D.C., 2007. SHARAD sounding radar on the Mars Reconnaissance Orbiter. J. Geophys. Res. (Planets) 112, 5. http://dx.doi.org/10.1029/2006JE002745.

Smith, D.E., Zuber, M.T., Frey, H.V., Garvin, J.B., Head, J.W., Muhleman, D.O., Pettengill, G.H., Phillips, R.J., Solomon, S.C., Zwally, H.J., Banerdt, W.B., Duxbury, T.C., Golombek, M.P., Lemoine, F.G., Neumann, G.A., Rowlands, D.D., Aharonson, O., Ford, P.G., Ivanov, A.B., Johnson, C.L., McGovern, P.J., Abshire, J.B., Afzal, R.S., Sun, X., 2001. Mars Orbiter Laser Altimeter: experiment summary after the first year of global mapping of Mars. J. Geophys. Res. 106, 23689–23722. http://dx.doi.org/10.1029/2000JE001364.

Tanaka, K.L., 2000. Dust and ice deposition in the martian geologic record. Icarus 144, 254–266. http://dx.doi.org/10.1006/icar.1999.6297.

Tanaka, K.L., Kolb, E.J., 2005. Geologic Mapping of the Polar Regions of Mars: Preliminary Results and Climate Implications. Open File Report 2005-1271 U.S. Geological Survey.

Tanaka, K.L., Rodriguez, J.A.P., Skinner, J.A., Bourke, M.C., Fortezzo, C.M., Herkenhoff, K.E., Kolb, E.J., Okubo, C.H., 2008. North polar region of Mars: advances in stratigraphy, structure, and erosional modification. Icarus 196, 318–358. http://dx.doi.org/10.1016/j.icarus.2008.01.021.

Tanaka, K.L., Scott, D.H., 1987. Geologic Map of the Polar Regions of Mars. Miscellaneous Investigations Series Map I-1802-C U.S. Geological Survey.

Tanaka, K.L., Skinner, J.A., Hare, T.M., 2005. Geologic Map of the Northern Plains of Mars. Sci. Invest. Map 2888 U.S. Geological Survey.

Thomson, B.J., Bussey, D.B.J., Neish, C.D., Cahill, J.T.S., Heggy, E., Kirk, R.L., Patterson, G.W., Raney, R.K., Spudis, P.D., Thompson, T.W., Ustinov, E.A., 2012. An upper limit for ice in Shackleton crater as revealed by LRO Mini-RF orbital radar. Geophys. Res. Lett. 39, 14201. http://dx.doi.org/10.1029/2012GL052119.

Watters, T.R., Campbell, B., Carter, L., Leuschen, C.J., Plaut, J.J., Picardi, G., Orosei, R., Safaeinili, A., Clifford, S.M., Farrell, W.M., Ivanov, A.B., Phillips, R.J., Stofan, E.R., 2007. Radar sounding of the medusae fossae formation Mars: equatorial ice or dry, low-density deposits? Science 318, 1125. http://dx.doi.org/10.1126/science.1148112.

Zhang, Z., Hagfors, T., Nielsen, E., Picardi, G., Mesdea, A., Plaut, J.J., 2008. Dielectric properties of the Martian south polar layered deposits: MARSIS data inversion using Bayesian inference and genetic algorithm. J. Geophys. Res. (Planets) 113, 5004. http://dx.doi.org/10.1029/2007JE002941.

Zhang, Z., Nielsen, E., Plaut, J.J., Orosei, R., Picardi, G., 2009. Ionospheric corrections of MARSIS subsurface sounding signals with filters including collision frequency. Planet. Space Sci. 57, 393–403. http://dx.doi.org/10.1016/j.pss.2008.11.016.

Zou, H., Nielsen, E., 2004. Methods for Obtaining Electron Density Profiles from MARSIS Ionograms and Derivation of Parameters Characterizing the Profiles. Internal Document MPAe-W-485-04-01 Max Planck Institut für Sonnensystemforschung.